HUMBOLDT-UNIVERSITÄT ZU BERLIN
MATHEMATISCH-NATURWISSENSCHAFTLICHE FAKULTÄT
INSTITUT FÜR PHYSIK

Characterization of the DECAL sensor - a CMOS MAPS prototype for digital electromagnetic calorimetry and tracking

Masterarbeit

zur Erlangung des akademischen Grades
Master of Science (M. Sc.)

eingereicht von: Lucian Fasselt
geboren in: Duisburg

Gutachter/innen: Prof. Dr. Cigdem Issever
Dr. Klaus Mönig

Eingereicht am Institut für Physik der Humboldt-Universität zu Berlin am: ....

Abstract

The DECAL sensor is a fully depleted monolithic active pixel sensor (DMAPS) prototype for digital electromagnetic calorimetry and tracking. Its 64×64 pixels with a pitch of 55 µm are fabricated in the modified TowerJazz 180 nm CMOS imaging process using a 25 µm epitaxial silicon layer. The sensor readout at 40 MHz is configurable in counting the sum of particles passing through the pixels grouped in either strips or pads. Sensor tests with sources of americium-241 and strontium-90 as well as with an X-ray tube are presented. The uniformity of the pixels is shown, allowing the summation of counts across all pixels. A characterization of the sensor is obtained through X-rays in the energy range of 4 to 60 keV. Two stand-alone energy calibration methods are developed and agree with each other. The signal height per photon energy is obtained to be $a = 5.54 \pm 0.37\,\mathrm{mV/keV}$ which corresponds to a conversion gain of $\mathrm{c_g} = 19.95 \pm 1.32\,\mathrm{\mu V/e^-}$. The relative energy resolution for photon absorption yields $\sigma_{\mathrm{E}}/\mathrm{E} = 12.2 \pm 3.5\%$. The absolute counts observed with the DECAL sensor agree with expectations and substantiate the assumption of a fully depleted epitax. Building upon the sensor characterization described in this thesis, further tests are proposed that could pave the way for the design of a multi-layered digital calorimeter prototype.

Contents

List of Figures

List of Tables

1. Introduction

Calorimetry is the experimental field of energy measurement. A traditional approach is to measure the heat transfer of a process through a temperature increase. In high energy physics experiments, environments of extreme energy densities are created and calorimeters require a fine spacial segmentation to distinguish the energy measurements of nearby particles. The Large Hadron Collider (LHC) is designed to accelerate protons up to the energy of 7 TeV, which corresponds to velocities of 99.9999991% of the speed of light. Taking the low proton mass into account, the energy of one such proton is comparable to the kinetic energy of a flying mosquito, too low to produce a measurable temperature change in a medium. New detection concepts for calorimetry have been developed that rely on scintillation, ionization or the formation of electron-hole pairs in semiconductors. They require a precise detection of light or charge rather than a temperature change. Driving advances in material physics were the fabrication of pure scintillators, noble liquids, semiconductors and Cherenkov radiators. They came along with important inventions for photon detection such as the photomultiplier tube or photon wavelength shifters [1]. High energy particle collisions produce many primary and secondary particles. While hadrons penetrate large thicknesses of absorbers, electrons and photons have a much lower penetration depth. Consequently, there is usually different subdetectors for hadronic and electromagnetic calorimetry. An electromagnetic calorimeter (ECAL) detects the energy of electromagnetically interacting particles through the formation of secondary particles and their energy depositions. A well functioning ECAL must therefore favor the emission of secondary particles as well as measure their energy. Different concepts of subdetectors use either two different materials for that (sampling) or combine them in one active medium (homogeneous calorimeter).

The idea of a digital electomagnetic calorimeter (DECAL) relies on counting secondary particles rather than measuring their energy deposition. Simulation studies identified that an improvement in energy resolution could be achieved [2]. Section 2 summarizes the fundamental particle matter interactions crucial to understand electromagnetic calorimetry and then moves on to discuss existing and potential detector concepts. Advances in the silicon sensor technology have lead to the design of a Depleted Monolithic Active Pixel Sensor (DMAPS). Its small sensitive pixel size offers high segmentation in all three dimensions of order $10 - 60\,\mu\text{m}$. It also keeps the charge collection time short and has already improved over time in radiation hardness while providing the potential to keep the costs for large detectors affordable. These factors have made DMAPS a potential technology for the implementation of a DECAL. The development of its technology as well as the description of the specific design of the DECAL sensor is described in section 3.

The main goal of this thesis is to characterize the signal formation in the DECAL sensor when being exposed to X-rays. For that, the sensor operation without incident particles has to be understood first. A focus is set on finding the optimal measurement parameters for a good signal-to-noise ratio (SNR), maximising the time in which the sensor is sensitive and testing the homogeneity among pixels. All these tests are described in section 4. During testing, two undesired effects have been found that show a dependence among pixels and restrict the time sensitivity. They are described together with a workaround solution of how to ensure stable sensor operation. This enabled radioactive source tests using strontium-90 and americium-241 that were performed at the laboratories of Humboldt University in Berlin and of Deutsches Elektronen-Synchrotron (DESY) in Zeuthen. Their signal formation, as discussed in section 5, motivated the undertaking of further measurements with an artificial X-ray source. This offers high photon fluence and variable photon energies. A measurement campaign with an X-ray source making use of the fluorescence of six different target materials has been organized and performed at the Rutherford Appleton Laboratory (RAL), UK. The high photon fluence and the comparison with a different X-ray detector allowed characterization of the DECAL sensor in section 5.3: The signal height formation is elucidated in the photon energy range of $4 - 60\,\text{keV}$ via two stand-alone calibration methods. The latter method includes a description of the energy spectra obtained with the DECAL sensor over the whole energy range. This allows us to estimate the energy resolution for photon absorption. Finally, the absolute number of counts is compared to expectations and gives insight into the size of the depletion zone in the pixels. Based on the discussion of the sensor characteristics, section 6 presents an outlook on further tests to be performed and how the results may enter a new chip design. With a new generation of the chip a multi-layer calorimeter prototype could be built.

2. Electromagnetic calorimetry

This chapter elucidates those fundamental interactions between particles and matter in section 2.1 that allow the functioning of an electromagnetic calorimeter (ECAL). The processes of bremsstrahlung and pair production are crucial for the formation of electromagnetic showers. The characteristic shape of electromagnetic showers is explained. An ECAL stops electrons and photons that are produced as secondary particles and detects their energy deposition. Hadrons can penetrate larger distances even in dense material and are stopped outside of the ECAL in a hadronic calorimeter (HCAL) that is thicker than an ECAL. Focusing in this thesis on electromagnetic calorimetry, a description follows on existing ECAL systems (section 2.2) as well as on the idea of the digital character of calorimetry (section 2.3).

2.1. Particle interactions in silicon for electromagnetic shower formation

Heavy charged particles in silicon

Charged particles lose energy through ionization when passing through matter. For charged particles heavier than electrons the mean energy loss in unit $\mathrm{eV\,g^{-1}\,cm^2}$ is described by the Bethe-Bloch formula

$$-\left\langle \frac{dE}{dx} \right\rangle = K z^2 \frac{Z}{A} \frac{1}{\beta^2} \left(\frac{1}{2} \ln \frac{2 m_e c^2 \beta^2 \gamma^2 T_{\max}}{I^2} - \beta^2 - \frac{\delta(\beta\gamma)}{2} \right) \tag{1}$$

using

K	$4\pi N_A r_e^2 m_e c^2 = 0.307\,075\,\mathrm{MeV\,cm^2\,mol^{-1}}$
z	charge number of the incoming heavy particle
Z, A	atomic number and mass of absorber (14 and 28 for silicon)
β	velocity of the incoming heavy particle in proportion to the speed of light
γ	Lorentz factor $\frac{1}{\sqrt{1-\beta^2}}$
I	mean excitation energy (137 eV for silicon)

and the maximum energy transfer in a single collision of a particle with mass M

$$T_{\max} = \frac{2 m_e c^2 \beta^2 \gamma^2}{1 + 2\gamma m_e/M + (m_e/M)^2}. \tag{2}$$

Equation (1) is accurate within a few percent in the range of $0.1 \lesssim \beta\gamma \lesssim 1000$ [3]. Its most important characteristic is the formation of a minimum for $\beta\gamma \approx 3$ regardless of the absorber material. The corresponding energy loss is called the one of a minimum ionizing particle (MIP). For detector systems it is crucial to be able to resolve the energy loss of a MIP. For lower energies the mean energy loss runs with $\beta^{-\alpha}$ with $\alpha \approx 1.4 - 1.7$, meaning that it falls with increasing energy until the minimum is reached. At higher energies the logarithmic term leads to a rise until it is attenuated through the so-called density effect correction $\delta(\beta\gamma)$. Physically this is explained by a polarization of the absorber medium rather than an increase of the ionization zone. Interestingly, the material type only enters eq. (1) weakly through the logarithmic contribution of I and the the ratio of Z/A which lies close to 0.5 for most elements.

For incident pions of 500 MeV the energy loss distribution in silicon absorbers of different thicknesses is shown in fig. 1a. It is described by the so called Landau straggling function whose most probable value increases with the silicon thickness. Note that the Bethe-Bloch formula describes the mean energy loss rather than the most probable value. For a 320 µm absorber the mean is around 37% higher than the maximum which is due to the long tail of the distribution. Mathematically, the mean of the Landau distribution diverges and only exists with a cut-off energy. A physical reason for high energy losses is the formation of δ-electrons that receive such a high momentum transfer from the incident particle, that they too can ionize the medium [4]. In application, few large energy loss events can lead to an unstable determination of the mean, while the most probable value is more reliably obtained [3]. Hence, a focus is set on the ratio of maximum to mean of the straggling functions, depicted in fig. 1b. The most probable energy loss - that is the maximum of each function- is around 20% larger for the 640 µm absorber than for the one of 80 µm thickness. The general dependence of the most probable energy loss in silicon scales logarithmically with the thickness according to

$$\Delta_{p,\mathrm{Si}} = \xi(\ln\xi + 20.97)[\mathrm{MeV}], \tag{3}$$

where $\xi = x\frac{KZz^2\rho}{2A\beta^2} = 0.17887\frac{x}{\beta^2}$ and the density of silicon $\rho = 2.33\,\mathrm{g\,cm^{-3}}$ are introduced and x is in unit cm [4]. The above equation is valid for relativistic heavy particles with $\frac{p}{m} = \beta\gamma > 30$, which correspond to momenta of $p_{\mathrm{proton}} > 28.1\,\mathrm{GeV/c}$ or $p_{\mathrm{pion}} > 4.2\,\mathrm{GeV/c}$. Consequently, the energy dependence drops out because in this regime β approaches one and $\Delta_{p,\mathrm{Si}}$ only depends on the silicon thickness. The following values are obtained

$$\Delta_{p,\mathrm{Si}}/x\,(x = 320\,\mathrm{\mu m}) = 283\,\mathrm{eV\,\mu m^{-1}} \tag{4}$$

$$\Delta_{p,\mathrm{Si}}/x\,(x = 80\,\mathrm{\mu m}) = 258\,\mathrm{eV\,\mu m^{-1}} \tag{5}$$

$$\Delta_{p,\mathrm{Si}}/x\,(x = 25\,\mathrm{\mu m}) = 237\,\mathrm{eV\,\mu m^{-1}} \tag{6}$$

and describe well the position of the maxima of the straggling function in fig. 1a, even though the pion momentum lies below the validity requirement mentioned above. Measuring the energy loss together with the charge and momentum allows for particle identification in large detector systems.

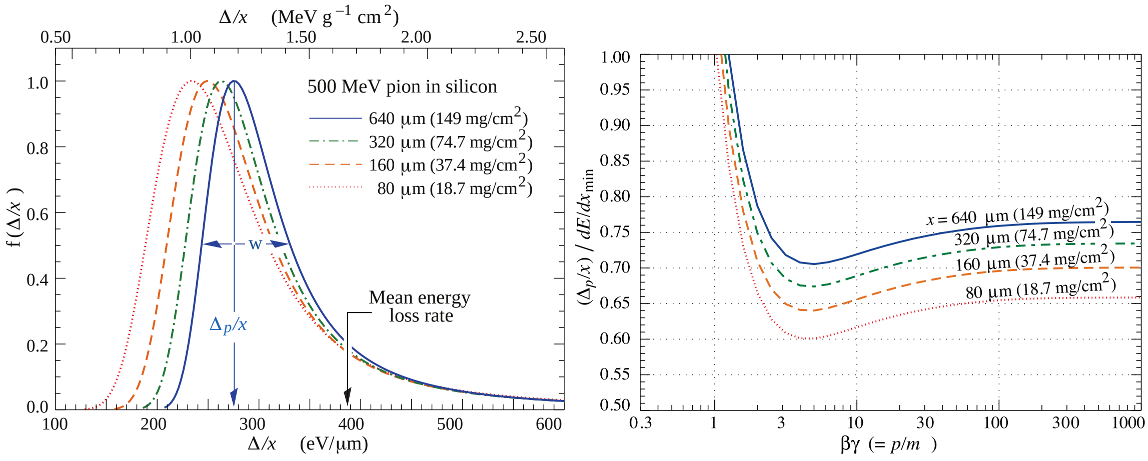

(a) (b)

Figure 1: Heavy charged particle energy loss for different silicon thicknesses. The straggling functions in a) describe the distribution of energy loss per unit length of incident 500 MeV pions. The distributions for different silicon thicknesses are each normalized by their most probable value, here denoted Δ_p/x. These values of Δ_p/x are plotted in b) as a function of $\beta\gamma$ which is proportional to the pion momentum. Here, all values are normalized by $388\,\mathrm{eV\,\mu m^{-1}}$, that is the mean energy loss of a MIP in silicon, also marked on the left plot. Both plots are adopted from [3].

Electrons in silicon

Charged particles with masses similar to the electron mass lose energy considerably through bremsstrahlung in addition to the process of ionization discussed above. Figure 2 depicts the steeper rise of bremsstrahlung compared to collision losses with increasing energy. A critical energy E_c can be defined as the particle energy at which the energy losses through ionization and bremsstrahlung are equal, that is the crossing of the lines in fig. 2. Using the formula

$$E_\mathrm{c} = 2.66 \left(\frac{Z X_{0g}}{A} \right)^{1.11} \tag{7}$$

the two processes coincide in silicon for a radiation length of $X_{0g} = 21.823\,\mathrm{g\,cm^{-2}}$ [5] at

$$E_\mathrm{c,Si} = 37.75\,\mathrm{MeV}. \tag{8}$$

Electrons of higher energy interact predominantly via bremsstrahlung, so that secondary particles are emitted. Once the electron energy approaches E_c the collision loss through ionization will stop the electron without further particle emission and the cascade of secondary particles comes to an end.

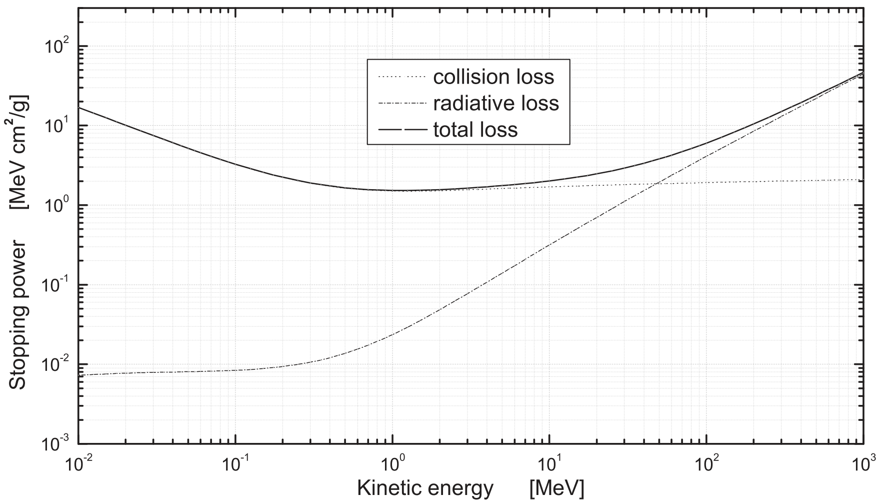

Figure 2: Stopping power of electrons traversing silicon. The radiative loss through bremsstrahlung increases almost linearly with energy in contrast to the collision loss through ionization. This causes an intercept of the two processes at a critical energy close to $E_{\mathrm{c,Si}} = 37.75\,\mathrm{MeV}$. The plot is taken from [4] and data is based on [6].

Photons in silicon

Photons when passing through matter can undertake three main interactions whose cross sections depend strongly on the photon's energy as well as the atomic number Z of the medium. For the case of 300 µm silicon the three processes are plotted over the incident photon energy in fig. 3a with an additional curve for the total absorption probability in cadmium telluride (CdTe). The material is frequently used in solar photovoltaic cells because of its larger absorption probability than silicon that comes from larger atomic numbers $Z = 46$ and 52 for cadmium and tellurium respectively. The dominant process at low photon energies, i.e. below 50 keV for silicon, is the absorption through the photoelectric effect under emission of an electron. The absorption is favoured when the photon carries an energy close to a binding energy of the electrons. As an example, K-shell electrons are most strongly bound as they are closest to the nucleus. The photon absorption probability peaks at their ionization energy. The photo effect depends strongly on the medium as it goes with Z to a power of around 5 [4].

Secondly, at intermediate energies until 10 MeV Compton scattering dominates. It is the elastic scattering of a photon from an electron in the medium whose atomic binding energy is negligible. The cross section of the process is proportional to the number of electrons in the absorber, from which follows that it scales linearly with Z. After the energy threshold of at least $2m_ec^2 = 1.022\,\mathrm{MeV}$ a photon can produce an electron - positron pair in the proximity of the Coulomb potential of a nucleus. The interaction with the nucleus is necessary to preserve momentum conservation. This

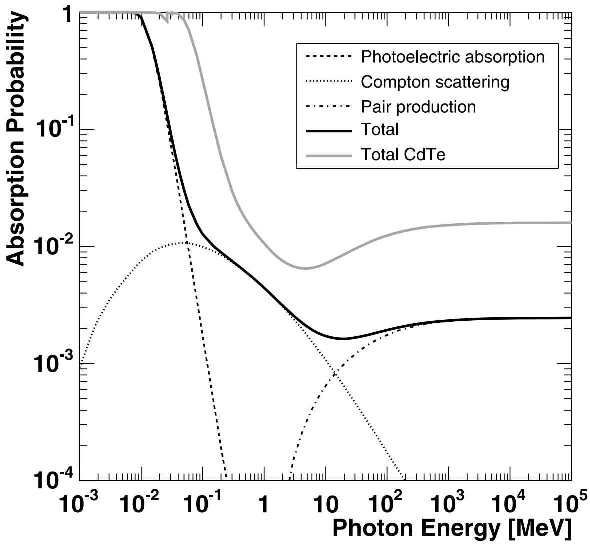

(a)

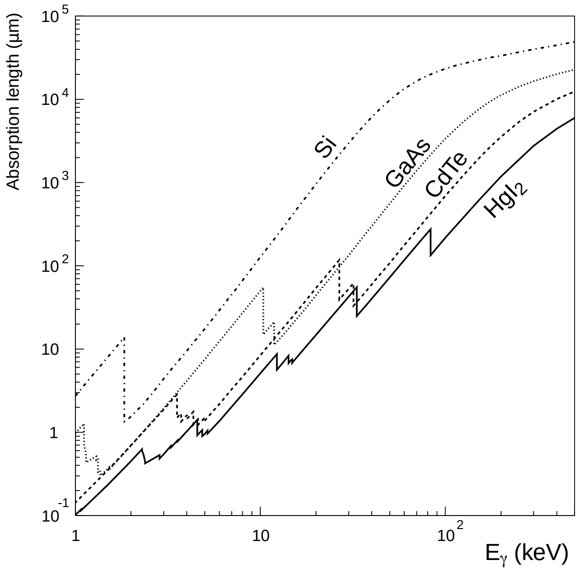

(b)

Figure 3: The photon absorption probability in 300 µm silicon is shown in a) for different energies. The energy ranges from 1 keV to 100 GeV. The photon absorption is shown in its three contributions as well as the total sum of them. For comparison, the total sum is shown for 300 µm CdTe whose photon absorption probability lies mainly one order of magnitude above the one of silicon. The absorption length in b) is larger for silicon compared to the other materials because of its smaller Z value and is here plotted in the X-ray energy range. The absorption edges arise from the photoelectric effect. Both plots are taken from [7], whose data is based on [8].

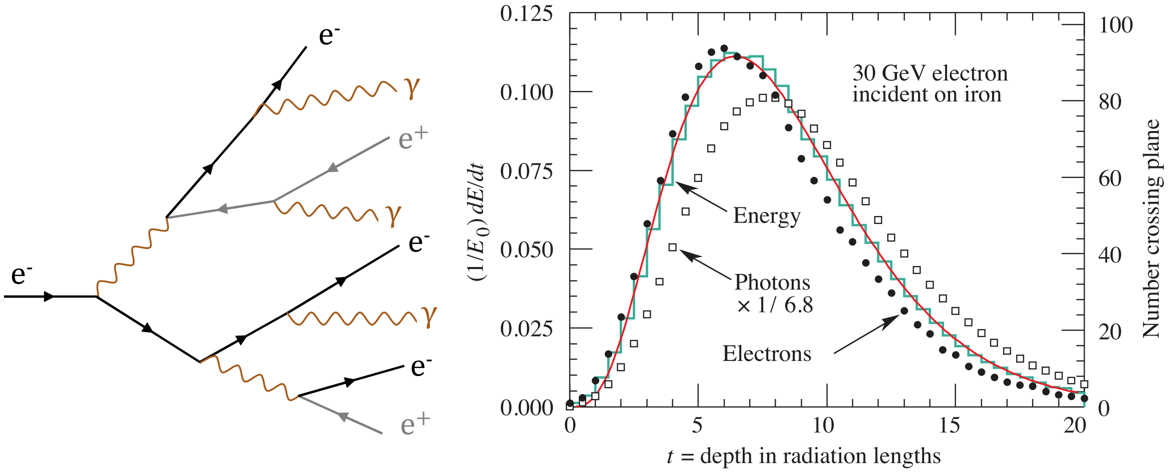

Figure 4: Electromagnetic shower formation as an illustration (**left**) and simulation of the number of secondary particles formed in iron (**right**) for a 30 GeV incident electron. The number of electrons is shown as circles and the number of photons is scaled down to the same area and depicted as squares. Only those particles with energy larger than 1.5 MeV are counted that are crossing planes at $X_0/2$ intervals. Additionally, the fractional energy deposition per radiation length is shown (green histogram with scale on the left axis). A gamma-function is fitted to it and shown in red. Plot is adopted from[3].

process - called pair production - dominates in silicon at energies higher than 15 MeV and its cross section is proportional to Z^2.

The description of these interactions build on a photon absorption rather than an energy loss unlike the case of massive particles. Following from the stochastic nature of the absorption, a photon beam loses intensity when traversing a material of thickness x according to the exponential decay

$$I(x) = I_0 e^{-x/\lambda} = I_0 e^{-x\mu}. \tag{9}$$

The attenuation length λ is material as well as energy dependent and the inverse of the attenuation coefficient μ. As described above, the photon absorption cross sections increase with Z. From this follows that the absorption length in silicon is larger than for materials of higher Z, as shown in fig. 3b. From the plot one can estimate that a 10 keV photon penetrates 100 µm silicon without absorption with a probability of roughly $e^{-1} = 37\%$. A 100 keV photon passes the same layer in even 99.6% of the cases. The comparison illustrates the energy dependence of the stochastic X-ray absorption process when using thin silicon.

Electromagnetic shower formation

The underlying particle matter interactions of photons and charged particles lead to the formation of electromagnetic showers - also called cascades. Their description is based on the radiation length X_0 which is material dependent. It characterises the length scale at which the energy of an incident electron is reduced by a factor of 1/e through bremsstrahlung on average. In a simple model, an incident electron, positron or photon of energy E_0 creates secondary particles of these same kinds until the critical energy E_c is reached. The cascade ends because the low energy charged particles are stopped through ionization and photons are being absorbed. An illustration of such a shower formation is presented in fig. 4. Furthermore, the number of electrons and photons as a function of the depth in iron simulated for an incident 30 GeV electron is shown. The number of electrons increases during the shower formation until it exhibits a maximum after

$$t_{\max} = \ln(E_0/E_c) + C_j, \tag{10}$$

where $C_{\mathrm{e}} = -0.5$ and $C_\gamma = +0.5$ for an electron and photon induced shower respectively and $t_{\max}$ is expressed in units of radiation length. Iron is characterized by $E_c = 21.68\,\mathrm{MeV}$ and the maximum number of electrons is exhibited at $t_{\max} = 6.73$. The deposited energy follows a gamma-function [3]. The lateral spread of the shower scales with X_0. On average 90% of the energy of the incident particle is deposited within a cylinder of Molière radius

$$R_M = X_0 \frac{E_s}{E_c}. \tag{11}$$

$E_s = 21.21\,\mathrm{MeV}$ is an energy scale and E_c the critical energy of the material [3]. All above simulations and formulas are valid for the description of average behaviour of electromagnetic showers. Single events can differ due to the statistical nature of the particle matter interactions.

2.2. Established electromagnetic calorimeter systems

Generally, an ECAL must be large enough in terms of radiation length to contain a whole electromagnetic shower and are thus typically 15-30 X_0 deep [3]. Equation (10) already indicates that the longitudinal length of a shower scales with ln(E), so that relatively compact detector designs are still feasible for high energetic particles. Containment of the whole shower prevents leakage of particles outside of the detector. Granularity defines the spacial resolution as the minimum separation of incident particles. One necessary requirement is a good discrimination between two closely spaced photons and those originated from the neutral pion decay. The photon identification and its precise energy reconstruction has been crucial to the discovery of the Higgs boson in its photonic decay via $H \rightarrow \gamma\gamma$ [4]. Overall, the relative energy resolution of calorimeters is parametrized as

$$\frac{\sigma_E}{E} = \frac{a}{\sqrt{E}} \oplus \frac{b}{E} \oplus c. \tag{12}$$

The contribution a is due to statistical fluctuations in the shower detection, the noise term b includes electronic noise and pileup and the constant term c dominates at high energies. It takes leakage, material inhomogeneities and the stability of calibration into account. There is two main concepts for an ECAL to be either sampling or homogeneous. A sampling ECAL consists of alternating layers of dense absorber material, usually with high atomic number, that generate the cascade process and of sensitive layers that detect the deposited energy. The detected fraction of the overall energy deposition in the active medium is called the *sampling fraction* and is usually proportional to the incoming particle energy E_0 [4]. The active medium can consist of a scintillator, a semiconductor, a noble liquid, or a gas ionization detector [3]. As the largest example, the A Toroidal LHC Apparatus (ATLAS) experiment has installed a lead-liquid argon (LAr) sampling ECAL with a barrel region and two endcaps with a thickness of more than 22 radiation lengths [9]. It is separated in three layers, of which the innermost layer is highly segmented to allow good spacial resolution of the shower formation and $\pi^0 - \gamma$ differentiation [10]. High energy photons or electrons emit secondary particles in the lead absorber plates. The charged particles then ionize the argon atoms in the LAr gap and the signal of the drifting electrons is collected by electrodes inside the gap. The choice of materials offers the advantage of radiation hardness however argon needs to be cooled to 88 K for keeping it liquid, which requires cryostats that enter the material budget. The ATLAS design energy resolution is

$$\frac{\sigma_E}{E} = \frac{10\%}{\sqrt{E}} \oplus \frac{170\,\mathrm{MeV}}{E} \oplus 0.7\% \tag{13}$$

and is achieved by keeping the temperature across the calorimeter stable and uniform [11]. As a second concept, a homogeneous ECAL combines the characteristics of absorber and sensitive material in one. Mainly used are scintillating crystals or non-scintillating Cherenkov materials [4]. The Compact Muon Solenoid (CMS) experiment relies on a lead tungstate ($PbW0_4$) scintillating crystal calorimeter whose light emission is detected by avalanche photo diodes (APD) or vacuum photo triodes (VPT) [12]. The compact design of the detector is necessary to fit inside a superconducting solenoid magnet. The energy resolution of the scintillators is excellent due to its high density and short radiation length as well as Molière radius. The signal is fast, as 80% of the light is emitted within 25 ns [10]. The CMS electron energy resolution was tested to be [11]

$$\frac{\sigma_E}{E} = \frac{2.8\%}{\sqrt{E}} \oplus \frac{120\,\mathrm{MeV}}{E} \oplus 0.3\%. \tag{14}$$

The excellent resolution comes with the cost of less radiation hardness because the light transmission decreases with irradiation while the scintillating mechanism remains unchanged [13]. Moreover, a homogeneous calorimeter comes with higher construction costs than a sampling one.

The requirements for future electromagnetic calorimeters in high energy physics are becoming more strict. The High Luminosity LHC (HL-LHC) expected to start operation in 2029 aims to reach an instantaneous and integrated luminosity of $7.5 \times 10^{34}\,\mathrm{cm}^{-2}\,\mathrm{s}^{-1}$ and $4500\,\mathrm{fb}^{-1}$ respectively. This is achieved by increasing the number of proton-proton collisions per bunch crossing: While for the current data taking in Run 3 up to 60 collisions are expected, it will go up to around 200 during HL-LHC. As the collisions happen within the same 25 ns bunch crossing, pileup increases. Pileup refers to multiple independent collisions being detected simultaneously. For the reconstruction of interaction vertices high granularity inside the calorimeters is beneficial for so called particle flow algorithms [14]. These algorithms combine different subdetectors for the overall particle identification, for example mapping particle tracks to the electromagnetic and hadronic showers.

Due to the increase in collision rate, the detectors have to withstand a much harsher environment and must be sufficiently radiation tolerant. To cope with that, the CMS Collaboration is currently preparing a new endcap High-granularity calorimeter (HGCAL) as a combination of silicon pixel sensors, scintillator tiles and absorbers [15]. The electromagnetic section will be a sampling calorimeter making use of $620\,\mathrm{m}^2$ of silicon sensors as active material providing high granularity. In this region the total radiation fluence will account for up to 10^{16} $\mathrm{n_{eq}cm}^{-2}$, too high for scintillators to withstand. Silicon pixel sensors are in wide use for tracking applications at the LHC and are entering again the upgrades of the inner trackers for ATLAS and A Large Ion Collider Experiment (ALICE). Due to lower requirements on radiation tolerance in ion-ion collisions, ALICE can already rely on monolithic pixel sensors rather than hybrid ones being the first LHC experiment to do so [16]. The technical description of various silicon sensor designs follows in section 3.1.

2.3. Digital electromagnetic calorimetry

The number of electrons and photons emitted in an electromagnetic shower has been described in section 2.1 with a simulation shown in fig. 4. The basic idea of a digital calorimeter system is to count the number of particles in different depths of radiation lengths and reconstruct the initial particle energy through the number of secondary particles. Similar to existing sampling calorimeters, dense absorber layers sustaining the shower formation are sandwiched between sensitive layers. Rather than measuring the energy deposition of secondary particles, the idea of a DECAL relies on counting them. The main motivation is the following. The energy deposition of charged particles through ionization fluctuates due to the statistic nature of the process as described in section 2.1. The width of the Landau straggling function quantifies the fluctuations around the most probable energy deposition. It is this statistical contribution that could be eliminated through the counting procedure of digital calorimetry and lead to an improvement of the statistical term $a/\sqrt{E}$ in energy resolution. At the same time a technology is sought that has lower costs than the current calorimeter concepts. Such a digital calorimeter would have the following requirements:

- **High granularity.** If two or more particles are incident in a pixel during one readout cycle their deposited charge adds up. For analogue readout the sum of depositions is measured and all traversing particles enter the energy determination. In a digital readout, an undercounting occurs if a pixel is saturated. Hence, the pixel size must be small enough to ensure an average pixel occupancy of $\ll 1$. For high particle fluences a pixel pitch of $< 100\,\mu m$ is required [2]. This high granularity is beneficial for particle flow algorithms connecting tracking and calorimeter subsystems.

- **Radiation tolerance.** The radiation tolerance must sustain the harsh environments such as planned for the HL-LHC. During its operation radiation hardness of up to $10^{16}\ n_{eq}cm^{-2}$ is expected in the innermost endcap calorimeter of CMS [15].
- **Low noise.** The detection of charged particles through ionization is essential. A signal of a MIP must be well separable from noise.
- **Quick charge collection and summation logic.** The charge collection time in the pixel must be less than $\sim 25\,ns$ to distinguish between bunch crossings and prevent dead time. The pixel hits must also be buffered and pipelined to storage with sufficient data rate to keep up with the 40 MHz collision rate.

Simulation studies have shown the potential of digital compared to analogue readout. An individual signal measurement is restricted to binary information regardless of the amplitude of deposited charge. A simulation in [2] has shown a 20% reduction of the statistical parameter a. The simulated improvement is so far restricted to particle energies below 100 GeV. Larger energies produce a higher particle density, hence saturation must be tackled by reducing the pixel size. However, smaller pixels increase the probability that the same particle passes through two pixels, leading to overcounting. A detector prototype has been built and tested that offers high granularity due to a pixel pitch of 30 µm but operates with an integration time of 640 µs, too slow for high energy particle applications [17]–[19]. Thus, the DECAL sensor was designed as a prototype to expand the testing of digital calorimetry to quick integration times suitable for a 40 MHz collision rate.

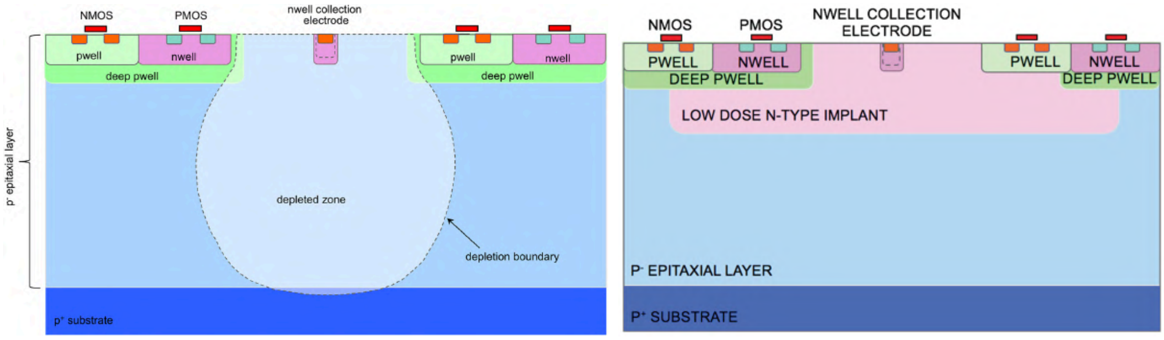

Figure 5: Pixel cross section for a standard and modified CMOS process. The standard process (**left**) is improved through a modified process (**right**) in terms of radiation hardness and a larger depletion zone. The improvement is due to the addition of an n-type implant with a gap at the pixel boundaries. The sketches are adopted from [20] and [21].

3. DECAL setup

This section summarizes the development of fully depleted monolithic active pixel sensors and motivates the choice of the DECAL sensor design in section 3.1. It goes on to explain the front end electronics of the DECAL pixel with a focus on its amplifier, shaper, tuning logic and its discriminator (section 3.2). The reconfigurable DECAL readout and data taking is explained in section 3.3.

3.1. A fully depleted monolithic active pixel sensor

Semiconductor pixel sensors often rely on silicon as the sensing material due to its low electron-hole pair production energy of 3.6 eV [7]. In comparison, ionization chambers are sensible to the ionization of its filling gas. The ionization of argon requires 15.7 eV and consequently results in a worse energy resolution than silicon devices [3]. At the basis of silicon pixel sensors, hybrid sensors are the state of the art in high energy detectors. Their sensitive pixels are manufactured separately from the readout electronics that are placed on a different chip. Sensor and readout circuit are then connected through bump bonds. Hybrid designs offer a choice of sensing materials such as CdTe or GaAs and are not restricted in the size and complexity of the readout circuits. In addition, its testing is easier because the readout is better accessible and even exchangeable. Nevertheless, hybrid designs come with disadvantages when facing the requirements of future high energy physics detectors. The demand of smaller pixel pitch sizes leads to more readout channels and more bump bonds driving the costs further for the bumping process. Aside from that, the bumping technology is pushed towards its diameter limit of around 10 µm for indium bumps [7]. In contrast, a Monolithic Active Pixel Sensor (MAPS) combines sensor and readout circuit on the same substrate. Its design is promising to reduce space occupation and the material budget. In particular, its large scale production is expected to stay within affordable costs, being based on the

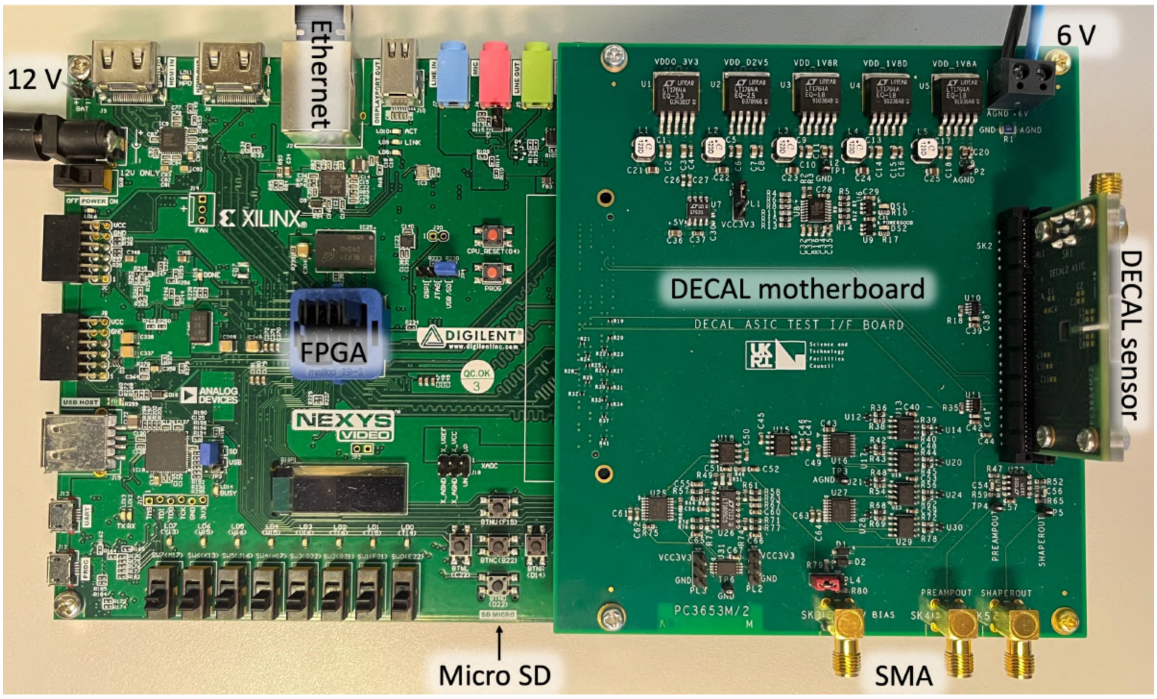

(a) Whole setup.

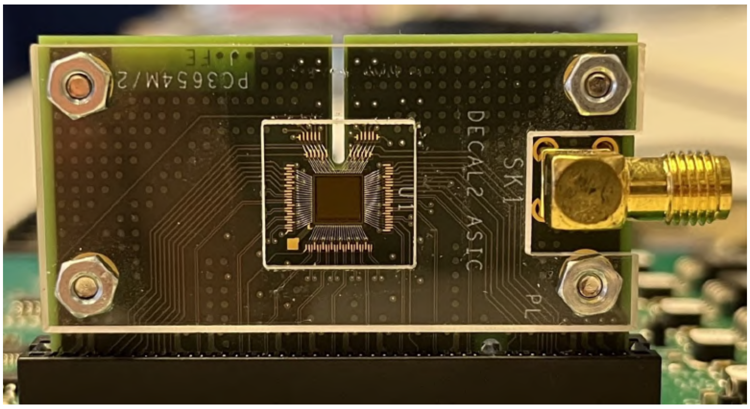

(b) Daughterboard.

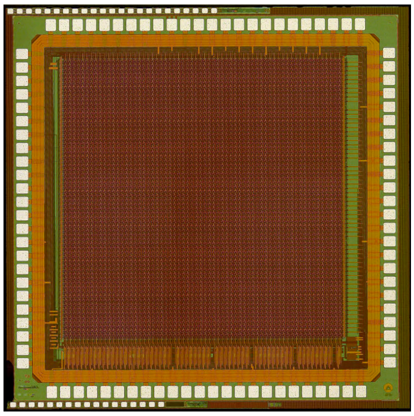

(c) Sensor.

Figure 6: The DECAL setup in (a) consists of an FPGA board, a motherboard and a daughterboard. The FPGA is firmware programmed via a micro SD card and communication to computer functions via ethernet. The DECAL sensor is wire-bonded to the daughterboard in (b). The microscopic view in (c) shows the sensor and the readout pads at all four sides, that are wire bonded to the daughterboard.

commercial Complementary metal-oxide-semiconductor (CMOS) technology that is widely used in industry for visible light applications, such as digital cameras [7], [22]. In early examples of MAPS the charge collection was based solely on the diffusion of charge carriers leading to slow collection times [23], [24]. The charge collection can be speeded up by applying either high voltage to the substrate or modifying the pixel design using high resistivity silicon. The pixel cross sections in fig. 5 show the choice of the modification compared to a standard process. The addition of the n-type implant increases the depletion region and thus favors through its higher electric field the drift of charge carriers rather than diffusion [25]. Simulation studies using Technology Computer Aided Design (TCAD) compared the modified process with two further revisions - either an extra deep p-well or a gap in the n- layer [26]. Both additions show a full depletion of the silicon epitax, hence introducing DMAPS. Their charge collection time is reduced by at least a factor of two before and after irradiation with a fluence of 10^{15} $n_{eq}cm^{-2}$. The unit compares the irradiation with the number of 1 MeV neutrons on a 1 cm^2 area of silicon. During 25 ns all created charges are collected, which is an improvement to the modified process. A higher radiation tolerance is achieved, shown by a three times higher collected charge after irradiation. The modified process is radiation harder and thus more applicable for environments such as the HL-LHC which is planned to start in 2029. Challenging for MAPS is the limited space that restricts the readout complexity in terms of numbers of transistors. Particles passing through thinner epitaxial layers create less electron-hole pairs, which in turn yield a lower charge collection. Only low noise will enable a good SNR and has to be kept low under irradiation. These challenges are being probed in current research projects mainly focusing on the application of DMAPS in tracking such as MALTA [27] or ALPIDE [28]. The DECAL sensor is a reconfigurable DMAPS prototype for both tracking and digital calorimetry. It is a 64×64 CMOS pixel array with a pixel pitch of 55 µm. An earlier variant has been fabricated in a standard TowerJazz 180 nm optical process with 18 µm silicon epitax while the current version under investigation in this thesis is built via a modified process with a 25 µm epitaxial layer [20].

3.2. Integrated pixel front-end electronics

The monolithic DECAL front-end circuit is fully integrated in each pixel and its schematic is shown in fig. 7. Starting from the collection diode biased through the resistor R_1 it comprises an amplification, shaping and discrimination unit - from left to right. The optimal goal is to collect all deposited charge, maximising SNR while keeping the rise time short and sampling the shaped peak at its maximum value. Some demands oppose each other, so a compromise is found for optimization. In order to understand the signal processing the individual units are discussed separately with the help of simplified circuits. The DECAL readout is presented in detail in [29] and general background on readout electronics can be found in [30], [31]. The presented calculations follow the argumentation of [32].

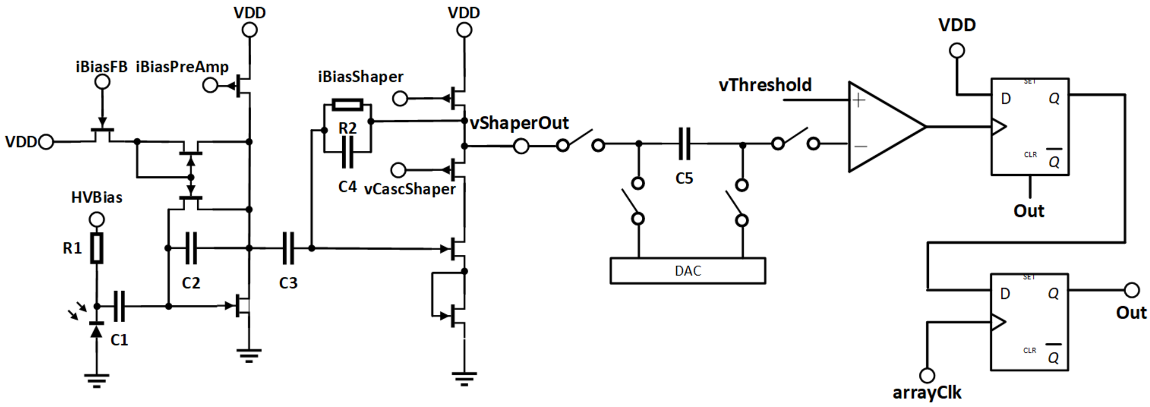

Figure 7: Fully integrated front-end of a DECAL pixel, including the amplifier, shaper and discriminator units.

Amplifier

Each pixel comprises a charge-sensitive amplifier that can be simplified by the circuit in fig. 8a. An input voltage pulse induces a step increase in the amplifier output through the following mechanism: The voltage gain A is positive and defined as the amplification from input to output voltage as

$$v_\mathrm{o} = -Av_\mathrm{i}. \tag{15}$$

The DECAL capacitor $\mathrm{C_2}$ acts as the feedback capacitor $\mathrm{C_f}$ and connects output and input. The voltage difference across $\mathrm{C_f}$ is

$$v_\mathrm{f} = v_\mathrm{i} - v_\mathrm{o} = (1+A)v_\mathrm{i}. \tag{16}$$

Under the assumption that all of the input charge Q_i is deposited onto the feedback capacitor, the effective input capacitance yields

$$C_\mathrm{i} = \frac{Q_\mathrm{i}}{v_\mathrm{i}} = \frac{Q_\mathrm{f}}{v_\mathrm{i}} = \frac{C_\mathrm{f} v_\mathrm{f}}{v_\mathrm{i}} = (1+A)C_\mathrm{f}. \tag{17}$$

From this the voltage output gain in terms of input charge is obtained as

$$A_Q = \frac{dv_\mathrm{o}}{dQ_\mathrm{i}} = -\frac{A}{C_\mathrm{i}} = -\frac{A}{1+A}\frac{1}{C_\mathrm{f}}. \tag{18}$$

For values of $A \gg 1$, that is accomplished when $C_\mathrm{i} \gg C_\mathrm{f}$, the output voltage amplification is dominated by the factor $1/\mathrm{C_f}$. For DECAL a large amplification is desired, so $\mathrm{C_2}$ should be chosen relatively low. From this perspective, the segmentation of the sensor and readout to small strips or pixels contribute to a large gain, because the capacitances shrink with it [33]. However, a low feedback capacitance will increase the rise time, so typical values chosen are 4-30 fF [7] and in the DECAL sensor $\mathrm{C_2} = 3.75\,\mathrm{fF}$

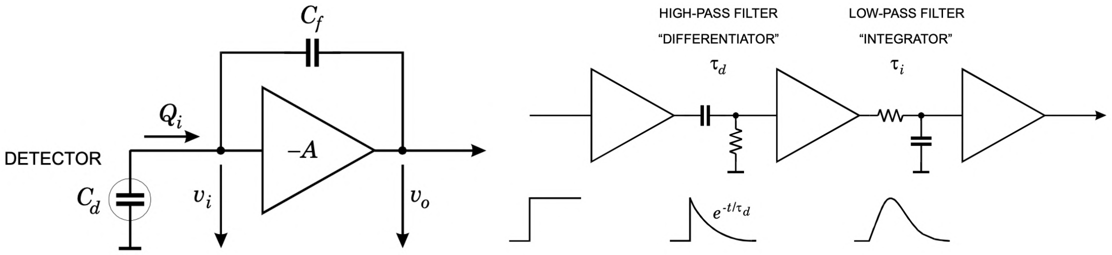

(a) A charge-sensitive amplifier.

(b) A CR-RC shaper.

Figure 8: A simplified amplifier and shaper circuit are shown. Schematics are adopted from [32].

was selected. Important for the voltage output is also the detector capacitance C_d, that is labelled C_1 in the DECAL schematic. The pixel charge Q_p distributes over C_d and the effective input capacitance C_i. The charge ratio

$$\frac{Q_\mathrm{i}}{Q_\mathrm{p}} = \frac{Q_\mathrm{i}}{Q_\mathrm{i} + Q_\mathrm{d}} = \frac{C_\mathrm{i}}{C_\mathrm{i} + C_\mathrm{d}} \tag{19}$$

approaches unity if C_i dominates over C_d, giving a maximal voltage output v_o. The discharging time constant of C_d determines the rise time of the amplifier and depends on the input resistivity

$$\tau_\mathrm{A} = R_\mathrm{i} C_\mathrm{d} = \frac{C_\mathrm{d}}{\omega_o C_\mathrm{f}}. \tag{20}$$

As opposed to the demand of a large gain in eq. (18), where a low feedback capacitance increases the gain and also SNR, here a large value of C_f is beneficial to keep the rise time short.

Shaper

The step-like voltage increase defined by the amplifier is shaped through a CR-RC unit of which a simplified view is shown in fig. 8b. The use of a capacitor and a resistor and their reverse positioning in the two filter steps explain the naming CR-RC. The shaper is required to reduce noise and separate voltage pulses of different clock cycles, so the rise and fall time should be kept short. The time constant of the whole peak is defined through the high-pass filter and its decay time τ_d as illustrated in the simplified circuit. For the purpose of finding the maximal peak height, a smooth plateau is required to sample the signal close to its maximum. The rise time τ_i of the low-pass filter slows down the step increase into a smooth rise forming a plateau at the maximum.

For testing purposes, one DECAL pixel provides an analogue readout through SubMiniature version A (SMA) connectors of its preamplifier and its shaper output. The charge deposition of a 1064 nm laser in that test pixel has been studied before through the Transient Current Technique (TCT) [34]. The used laser has a focal spot size of $10 \times 10\,\mu m^2$ and can deposit charge in a single pixel. The decay time of the shaper output was found to be of order 100 ns.

Six bit tuning DAC and discriminator

The amplification and shaping happens in each pixel individually. Threshold variations among pixels are expected due to fluctuations in doping concentration, different geometric sizes of layers, oxide thickness and production variations of the transistors. The threshold voltage in the discriminator can only be set globally for all pixels. To align all pixels in their voltage baselines a six bit tuning DAC is implemented in each pixel. The six bit values enter the tuning DAC schematic in fig. 9 and consist of

- **bit 1** for masking or unmasking the pixel. This decides whether the shaper output is connected to the discriminator input through the transistors M1 and M2. A masked pixel is deactivated in the sense that its shaper output signal does not reach the discriminator.
- **Bit 2** defines the polarity of adding or subtracting to the shaper output. This decision is implemented via the transistors M3-M6, where positive polarity (calib_plus) stands for addition to the shaper output. This arrangement doubles the tuning range without having to add more transistors for amplification in the current mirror.
- **Bits 3 - 6** set the magnitude of the voltage shift. The four transistors M7-M10 act as a current mirror and are doubling the current from one transistor to the other. The transistors M11 to M17 are grouped in pairs and can be set externally via the four bits. Their choice decides whether the current from the upstream transistor is guided to ground or to the DAC output, generating a voltage through resistor R3. It is this voltage that is added or subtracted via the second bit setting.

The correct functionality of the tuning DACs is proven in section 4.1. The discriminator is fed by the shaper output after tuning and compares its voltage with the globally set threshold voltage. Only a binary information is stored, when the shaper output drops below the threshold. This way, the discriminator separates the analogue front-end from the digital processing that follows. It is synonymously referred to as comparator and its detailed implementation can be found in [29]. The time response of the entire pixel readout has been investigated already [34]. For charge deposition an infrared laser was used. An illuminated strip detects signal hits for each laser pulse within one 40 MHz clock cycle, indicating that the time response of passing the threshold voltage lies within 25 ns. Such quick timing is required in many high energy experiments.

3.3. Readout and data acquisition

Summation of the DECAL pixel counts in each strip is thoroughly discussed in [29] and its result summarized here. A summation architecture consisting of half- and full-adders

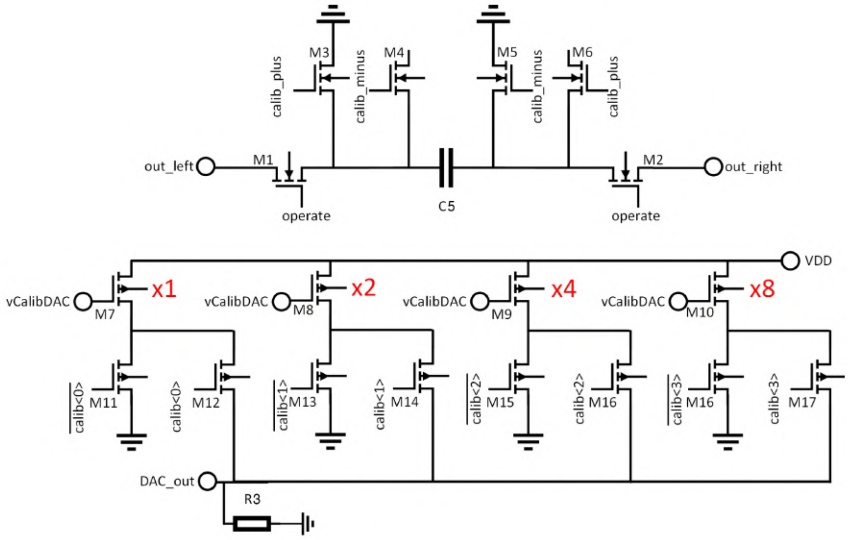

Figure 9: Tuning DAC schematic. The output of a four stage current mirror is added or subtracted to the shaper output for pixel tuning. The amplification stages indicated by multiples of two are marked in red. The magnitude and the sign of the voltage shift is set digitally through bit values as explained in the text in more detail. The schematic is adopted with slight changes from [29].

is chosen as a combination of a waterfall and a cascade summation logic. In a waterfall logic, a count in pixel 64 is added to the one of pixel 63, their sum to 62, and so forth. The number of parallel lines is equal to the bits needed to represent the maximum sum. In cascade logic two neighboring pixel counts are added, then two of such sums added, providing the sum of four pixels, then these add to a sum of eight pixels, and three more such additions complete the sum for 16, 32 and finally all 64 pixels. Introducing a counting limit of 15 hits per column reduces the summation time and number of parallel lines. The choice was made to combine the two approaches by using the cascade logic in blocks of 16 pixels and then add the resulting four blocks in waterfall logic. This keeps the summation time as low as 7.5 ns and makes use of 13 parallel lines and 388 gates. Each 16 pixel cascaded sum has a four bit representation, implementing the counting limit of 15 already at this stage. Also, the count limit after summing the four 16 pixel blocks is 15 at most. The mixed scheme allows the completion of the summation logic within one 25 ns clock cycle and fitting the parallel lines and gates inside the sensor design without having to remove pixels. The reconfigurable readout defines the processing of the column sums via low-voltage differential signaling (LVDS) output pads to the field-programmable gate array (FPGA) board. The two options are:

- **Strip-mode.** In strip mode all 64 pixels in one column are readout as one strip. A maximum of 3 hits per strip and clock cycle can be summed up, with the loss of information about which pixels have detected a hit. This mode is suitable for outer tracking applications as the 55 µm wide strips allow good space resolution.

Per strip the two bit sum is passed, meaning that for 16 strips a 32 bit number is passed via four 8 bit LVDS output pads. The two bit number represents whether 0, 1, 2 or at least 3 hits are detected.

- **Pad-mode.** In pad-mode 16 columns are grouped together. While the spacial resolution deteriorates compared to the strip-mode more counts can be read out. In each strip up to 15 hits can be detected, resulting in 240 hits per pad. The application is useful for calorimeters because many secondary particles can be detected per clock cycle. This way, strip saturation occurs only if 16 or more pixels detect a hit simultaneously. In calorimetry the requirements for spacial reconstruction are less strict and saturation under high occupancy is to be prevented. In detail, the four bit number per strip that represents up to 15 counts are summed across all 16 strips in one pad. To pass the maximal number of 240 hits, an 8 bit LVDS is needed per pad. Further, each strip provides an overflow bit, the sum of the overflows - 16 at most - is passed via a second 8 bit LVDS.

The correct functionality of the digital summation logic has been already verified in [35]. When referring to the geometry of the pixel matrix, a column or strip is the dimension over which the hit summation is conducted. Rows make up the other dimension. Currently, we are testing a single sensor which is wire bonded to a printed circuit board (PCB). The communication between DECAL sensor and computer functions via the Nexys Video FPGA board and follows the ROOT-based framework of ITk Strips Data Acquisition (ITSDAQ) [36].

4. Determination of measurement parameters

The DECAL setup as described in the previous section is examined for systematic effects. Their study is crucial to allow moving on to signal measurements in section 5. The general aim is to find reproducible measurement settings while minimizing noise contributions. The following issues observed during testing are approached: Emphasis is first placed on the pixel tuning for noise reduction in section 4.1. Later, the currents entering the pixel readout are being optimized (section 4.2). A voltage drift of the threshold voltage requires all pixels to be reset frequently. The description of this drift as well as the necessary reset to allow reasonable measurements follows in section 4.3. In the next preparatory step the heat generation of the sensor is examined with the aim to select reproducible and stable conditions for data taking (section 4.4). Finally, section 4.5 describes the broadening of the noise peak when unmasking all 64×64 pixels.

4.1. Pixel tuning with a six bit digital-to-analog converter

The electronics of each pixel contain a six bit Digital-to-analog converter (DAC) that produces a shift to the shaper output when entering the comparator and has been elucidated in section 3.2. Tuning is necessary because from fabrication the voltage output level varies among pixels and the threshold voltage can only be set globally for all pixels together. The aim of the tuning is to find the bit configuration per pixel that aligns the shaper outputs in the absence of a signal. The voltage baseline of the shaper output is found under the variation of the threshold voltage. Such a threshold scan is characterized by a noise peak, that is formed where the threshold voltage coincides with the voltage baseline. The width of the noise peak scales with the amplitude of fluctuations of the shaper output. For a single pixel its standard deviation is found to be 2.4 mV on average. Figure 10 shows the tuning through the $2^5 = 32$ configurations of an unmasked pixel that arise from the different possibilities to choose the latter five bits of the tuning DAC. The DAC configurations 0 to 15 correspond to a negative polarity, meaning that the shift is subtracted from the shaper output. Configurations 16 to 31 in turn have positive polarity, resulting in an addition of the shift. The magnitude of the shift is zero at configurations 15 and 16 and increments to both sides. Consequently, at the edges for configuration 0 the maximum shift is subtracted and for configuration 31 it is added. The linearity of the four bit shift is clearly visible. It is interesting to note that the drop between configurations 15 and 16 is due to the polarity change. Hence, adding and subtracting a shift of zero results in a slightly shifted voltage output. While a complete linear behaviour over the whole range would be optimal, the drop is preferred in the chip design because it leads to an overlap in the voltage range of both polarities. This overlap guarantees a coverage of the whole voltage range which would be amiss for a jump in the opposite direction.

The magnitude of the voltage shift is defined by the four latter bits and is proportional to a DAC calibration current. Hence, the current defines the covered voltage range

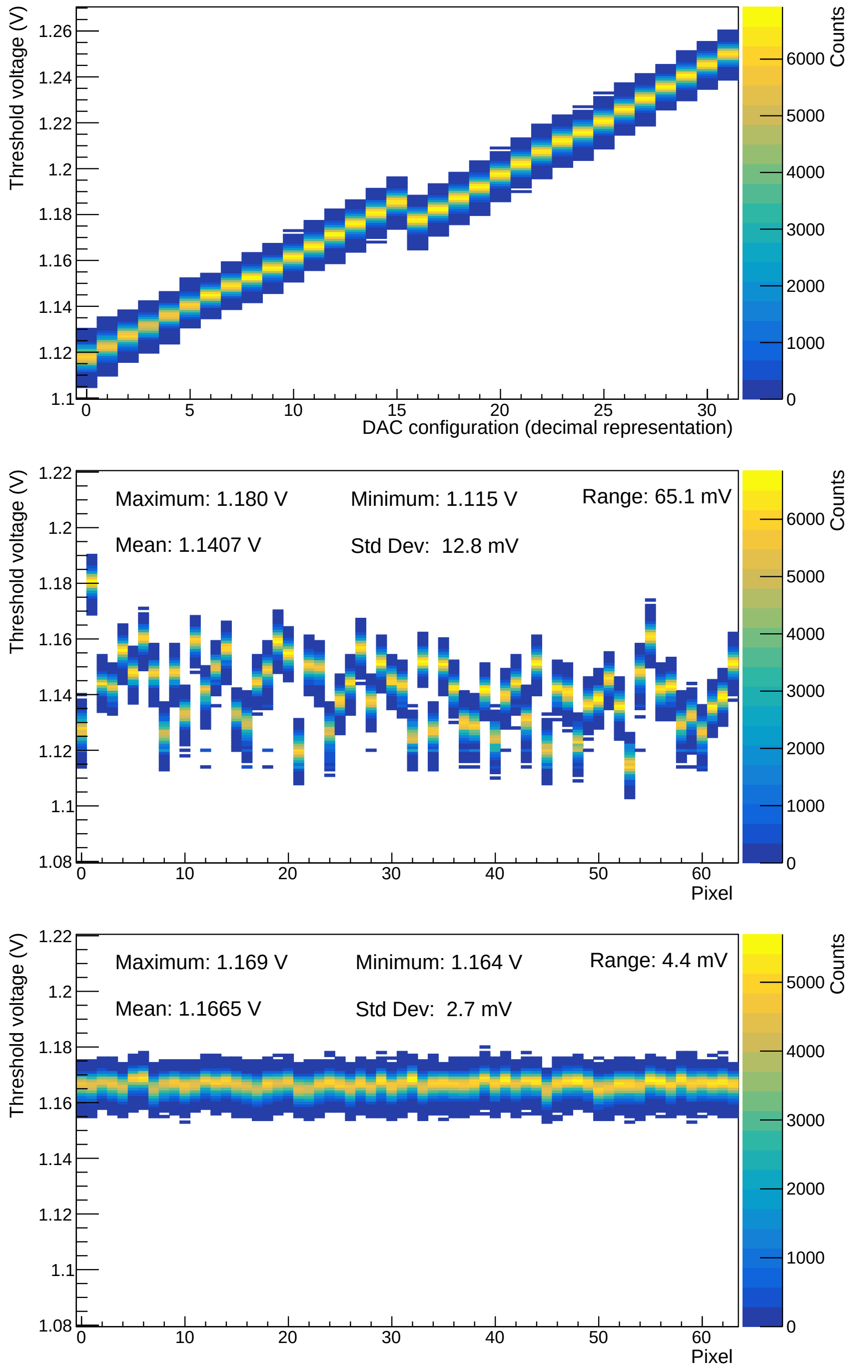

Figure 10: Pixel-wise tuning procedure. The noise peak of an unmasked pixel is tuned through all 32 possible DAC configurations (**top**). For each pixel the configuration is chosen whose mean is located closest to a nominal voltage value. A scan for 64 pixels in one row is displayed before (**middle**) and after tuning (**bottom**), reducing the range of peak positions by a factor of 15. Pixels from the other 63 rows are masked so that only counts from single pixels in one column are measured.

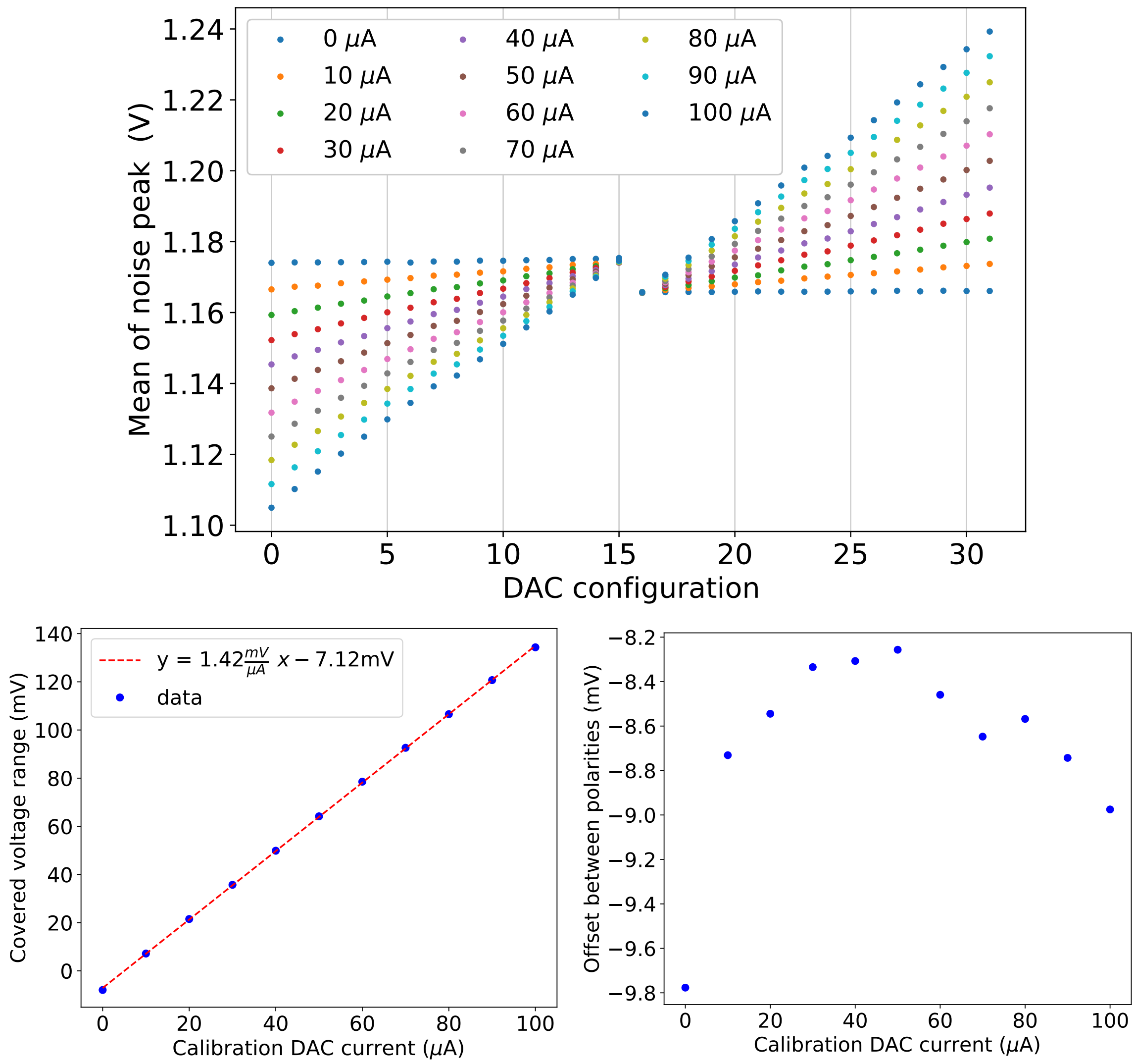

Figure 11: Variation of the calibration DAC current. The tuning of the mean noise peak position (**top**) depends on the value of the current with following two characteristics: The voltage range covered between the two extreme DAC configuration scales linearly with the current (**bottom left**). The offset between the two polarities (**bottom right**) shows no clear current dependence and evaluates to $8.67 \pm 0.41\,\mathrm{mV}$ on average.

between configuration 0 and 31 as well as the step size between adjacent configurations. These two effects entail opposing arguments as a higher current widens the covered voltage range that ensures all pixels to be tuned to the same nominal voltage. However, at the same time a smaller current leads to a smaller step size which improves the resolution of the tuning. Both effects are observed in fig. 11. The proportionality between the voltage range coverage and the DAC calibration current is well described by a linear fit. Its gradient of 1.42 mV/µA defines both the resolution as well as the voltage range. The offset between the polarities shows no clear dependence on the current and quantifies as -8.67 ± 0.41 mV on average. The uncertainty is the standard deviation of the sample.

For the purpose of tuning all pixels, a calibration DAC current of 100 µA is chosen because the corresponding voltage range spans over 135.0 mV according to the linear model. This range is necessary to be able to tune the means of the noise peaks of all 64×64 pixels to a global value. Figure 10 shows a threshold scan of a single row before and after tuning while pixels from other rows are masked. The range between two extreme noise peak positions is reduced from 65.1 mV to 4.4 mV. Most importantly, the projected sum of all pixels on the y-axis is described by a much reduced standard deviation. The tuning process reduces it from 12.8 mV to 2.7 mV. Altogether, the tuning allows the summation of pixel counts for a globally set threshold voltage. The tuning process as described above has been published in [37].

4.2. Current setting in pixel electronics

The setting of the following three currents in the pixel electronics is investigated for an interval of 0 to 600 µA. Their influence on the mean of the noise peak, the standard deviation and the maximum height are displayed in fig. 12. Based on this measurements the currents are characterized and their values selected:

- **Shaper bias current** I_{SB}**:** The shaper bias current enters as a transistor base bias in the shaper circuit. It shifts the shaper output voltage and thus the whole noise peak on the voltage axis. Only currents up to 200 µA are examined as higher currents shift the noise peak out of the measured voltage range. Also, it leads to a turn-on behaviour as the height peaks at 100 µA. This current is preferred because larger currents come along with a suppression of counts.

- **Preamplifier bias current** I_{PB}**:** The preamplifier bias current feeds the preamplifier circuit with a bias through a transistor. It generates a turn-on curve for the maximum of the noise peak. The mean position is not affected but the standard deviation rises approximately with the square root of counts. The amplification saturates around 100 µA justifying it to be the desired current value.

- **Feedback circuit bias current** I_{FCB}**:** It stabilizes the DC bias of the preamplifier. Currents up to 600 µA show no impact on the shape of the noise peak beyond statistical fluctuations. I_{FCB} is also being fixed at 100 µA.

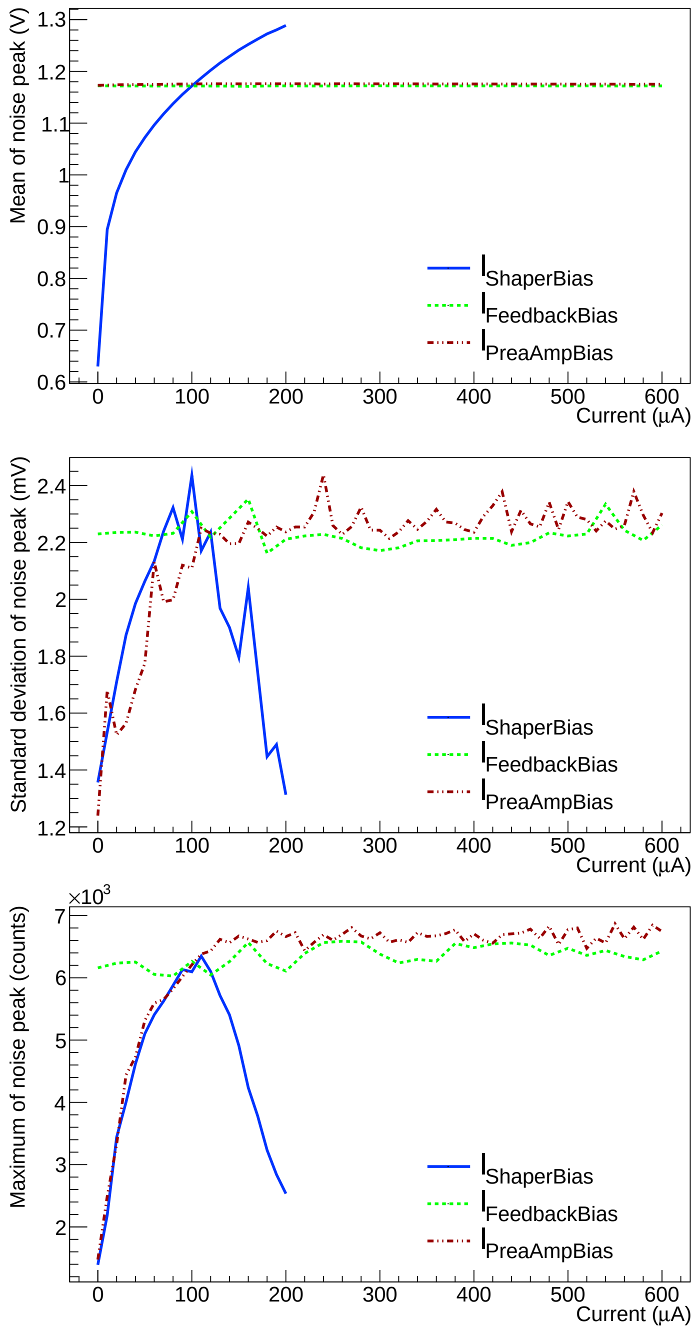

Figure 12: Current variation in the pixel electronics of the shaper bias current I_{SB}, the preamplifier bias current I_{PB} and the feedback circuit bias current I_{FCB}. Their influence on the shape of the noise peak of the pixels is studied - namely the mean position of the noise peak (**top**), the width described by the standard deviation (**middle**) and its maximum height (**bottom**). All values are averaged over the 64 pixels in one row.

All three current values are chosen based on how the noise peak is effected. Such a choice makes sense under the assumption that a charge collected from a signal is amplified and shaped accordingly. In the future the expected turn-on behavior for signals under I_{SB} and I_{PB} variation can be tested using a TCT setup. This allows to deposit charge in single pixels which is extremely useful since only one test pixel offers an analogue readout for comparison with the digital counts.

4.3. Mitigation of observed voltage drift through pixel reset

All pixels can be reset by disconnecting and subsequently reconnecting the shaper output to the comparator input. After applying a reset it is detected that the pixel voltage baseline drifts over time, which is an undesired behaviour. As the externally set threshold voltage can be kept constant, for optimal sensor operation the shaper output should stay at its baseline, too. A future design of the sensor is aimed to solve this issue. This undesired voltage drift can be quantified by the variation of the parameter here called *nsleep*. *Nsleep* defines the number of clock cycles that are waited between the reset of the pixels and the start of measurement taking. The larger *nsleep* the more time elapses for a voltage drift to occur. Figure 13 shows the mean of the noise peak under variation of *nsleep* for one pixel. For low values of *nsleep* the mean lies closely above the threshold voltage of 1.17 V which was chosen in the tuning process. Larger values of *nsleep* lead to a drift of the mean to lower voltages. This voltage drift is well described by a linear fit. The y-intercept b describes the voltage level just after reset and the gradient m the voltage drift. m is in unit V/clock cycle. V_{Drift} in unit mV/ms is obtained as

$$V_{Drift} = m \times 80 \times 10^6 \, \mathrm{ms}^{-1}. \tag{21}$$

The voltage drift differs between pixels and does not depend on the position in the chip geometry - its row and column number - as no pattern evolves in the heatmap in fig. 13. The histogram of the voltage drifts is characterized by a mean drift of 18.92 mV/ms. Interestingly, it shows outliers that lie up to seven standard deviations away from this mean value, such as the pixel shown as an example with the linear fit. These outliers cause a long tail in the histogram and are due to variations in the fabrication process, such as different doping concentrations, differing transistor and capacitor properties in the pixel readout.

In order to make sense of the DECAL measurements, a pixel reset has to be executed frequently. For this purpose the two variables *nsleep* and *maxcap* have to be specified. The time taken for the reset is measurable through the analog output of the test pixel and is measured to be 2.0 µs, that is 160 clock cycles. Setting *nsleep* to values of 300 clock cycles or higher results in meaningful threshold scans as no unexpected counts appear outside the noise peak that would appear for smaller values. Nevertheless, *nsleep* is chosen to be 1100 clock cycles to be large enough also for slower computers that are expected to have a larger latency time making the pixel reset longer. After these *nsleep* clock cycles are waited, the measurement process begins and is sensitive during *maxcap*

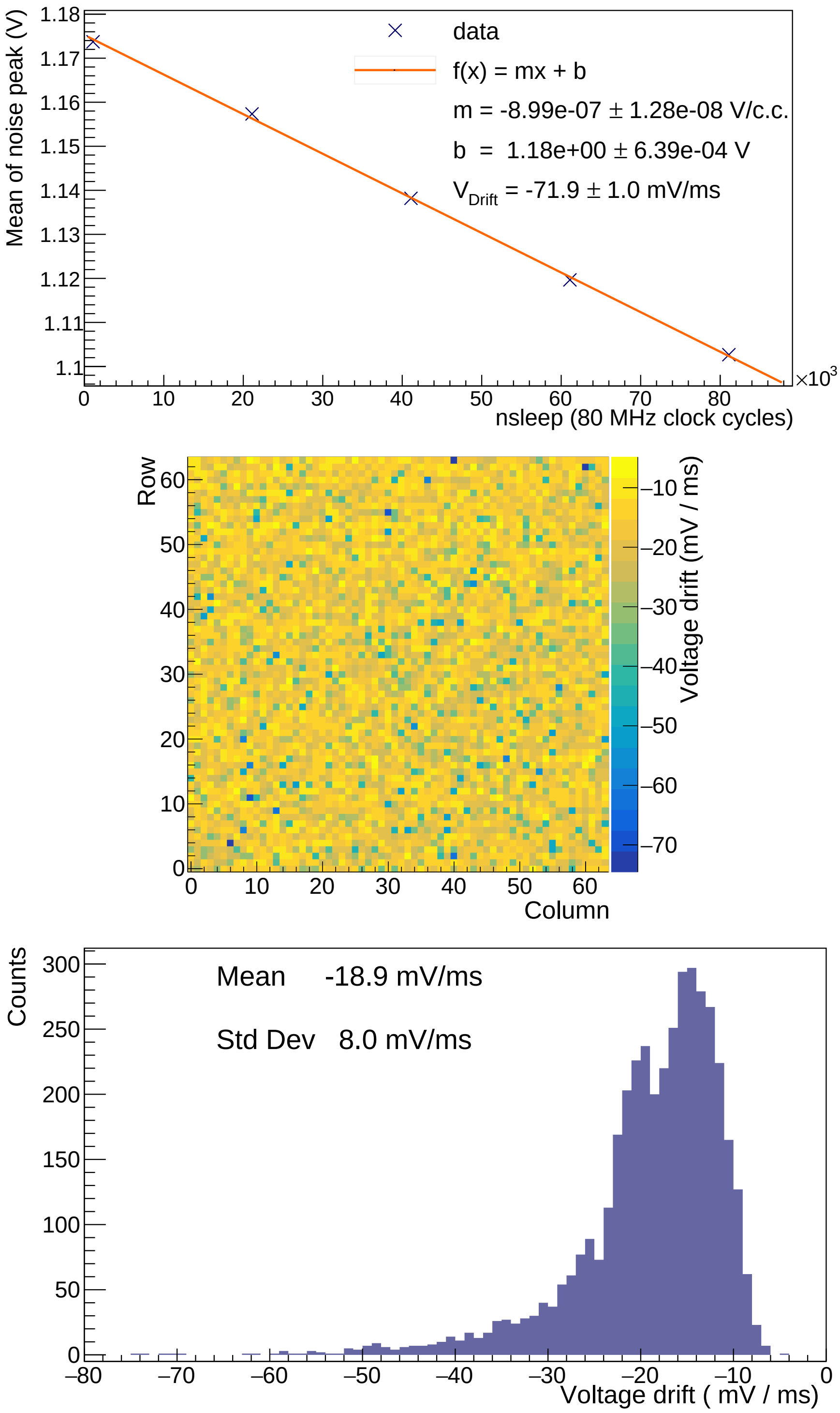

Figure 13: Voltage drift of each pixel. The voltage drift per pixel is determined by variation of the *nsleep* parameter and a linear fit to the mean of the noise peak as shown for the pixel in row 63 and column 40 (**top**). The drifts of all pixels are displayed as a heatmap over the chip geometry (**middle**) and as a histogram (**bottom**).

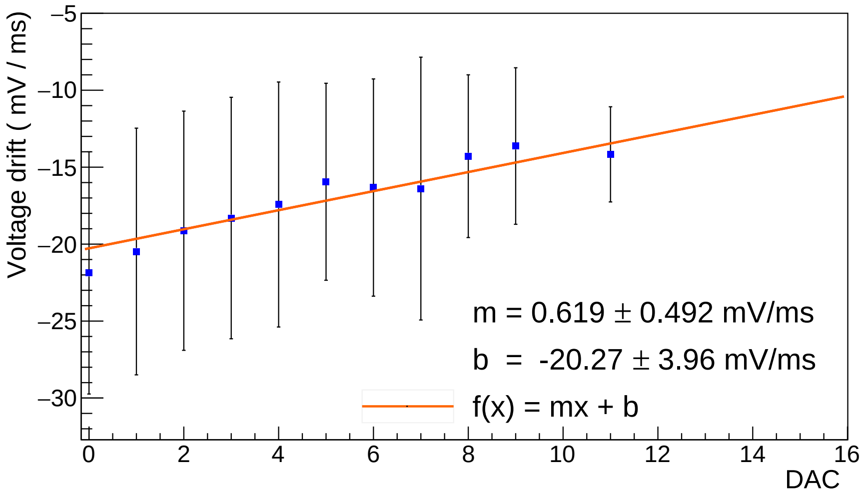

Figure 14: Voltage drift dependence on tuning DACs. The voltage drift values are plotted over the four bit value of the tuning DACs. Some DAC values - to the large end - are not chosen in the tuning process explaining the missing data points. The two different polarity settings are combined because no dependence on the drift is measured there. Error bars represent the standard deviation over the sample of pixels with the same DAC value.

clock cycles until another pixel reset is performed. As the voltage baselines of all pixels drift, *maxcap* should not exceed a value, that causes a voltage drift of more than 1 mV. This requirement stems from the fact that threshold scans are usually performed in steps of 1 mV. A value of $maxcap = 2000$ clock cycles is chosen from which the mean voltage drift will result to 0.73 mV at the time of completing 3100 waiting (*nsleep*) and measurement (*maxcap*) clock cycles. It is noted that the pixel reset is very time consuming, because it demands multiple communications between computer and FPGA board. While the pixel reset itself takes 2 µs, consecutive resets take 160 µs latency time in between. Consequently, for the measurement taking of 2000 clock cycles - that is 25 µs - at least 160 µs are needed, so that the sensor can be at most 15.6% sensitive of the time.

The cause of the voltage drift is explored based on the pixel schematic in fig. 7. The comparator is fed by the capacitor C5 whose voltage is expected to leak over time. The capacitor in turn is charged by the shaper output and a shift to this voltage is added through the six bit tuning DAC. The following sources for the voltage drift are investigated:

- **Shaper bias current** I_{SB}: Variations of I_{SB} have been discussed before (section 4.2), showing that the noise peak is shifted through a current increase. A follow-up investigation is whether the voltage drift depends on I_{SB}. For that, the voltage drift is determined according to the linear fit in fig. 13 under variations of the I_{SB}. No dependence between drift and this current is observed, meaning that different values of I_{SB} neither favor nor prevent the drift. It is nevertheless possible and so far remains untested, that I_{SB} itself decreases with time, causing the mean of the noise peak to shift according to fig. 12.

- **Tuning DACs:** The voltage shift through the six bit tuning DACs enters directly before the comparator input. It is measured that lower shifts lead to a larger voltage drift as can be seen from fig. 14. However, the dependency is too weak to explain the voltage drift of the outlier pixels. This measurement can be improved by determining the voltage drift of each pixel for all 32 DAC configurations. Here, only the one configuration per pixel is scanned that was chosen in the tuning process. As a consequence, some large DAC values are not populated. Lower uncertainties are to be expected from the improved analysis, however an explanation for the outlier drift values will still be pending.

The search for the clear cause of the undesired voltage drift remains ongoing. Its dependence on the tuning DAC value encourages to search for variations of the calibration DAC current. Generally, it is useful to check all currents for stability, bearing in mind that a falling shaper bias current I_{SB} is another potential cause for the voltage drift. A future submission of the chip is sought to resolve the voltage drift and aim for entire time sensitivity by not having to restrict the measurement clock cycles *maxcap* as a workaround.

4.4. Heat generation of the chip

Seeking reproducible measurements includes an analysis of the heat generation of the chip and whether measurements depend on the temperature. Figure 15 shows 1250 repetitive threshold scans of the same row during the time frame of 850 s. The upper (red) and lower (cyan) data points show the mean of the noise peak of two exemplified pixels, while the middle (blue) points represent the mean of the sum of the noise peaks over all 64 pixels in the row. An exponential decay describes the time evolution well with a time constant $\tau = -210.5\,\mathrm{s}$. The voltage $\Delta\mathrm{V} = 1.63\,\mathrm{mV}$ is the offset at the start of the measurement time relative to the equilibrium vale of $V_0 = 1166.18\,\mathrm{mV}$. As the threshold scans are typically applied in steps of 1.0 mV an offset of 0.5 mV is acceptable for the determination of the mean of the noise peak. According to the fit parameters the time after which the mean lies less than 0.5 mV above its equilibrium value calculates as

$$t_{0.5\,\mathrm{mV}} = \tau \ln \frac{0.5}{\Delta V} = 249.28\,\mathrm{s}. \tag{22}$$

To improve this minimum requirement, all measurements will be preceded by a repetitive threshold scan lasting 5 minutes during which heat is generated in the whole chip. This warm-up scan approaches thermal equilibrium and even reduces the voltage offset to

$$V_{300} = \Delta V e^{300\,\mathrm{s}/\tau} = 0.39\,\mathrm{mV}. \tag{23}$$

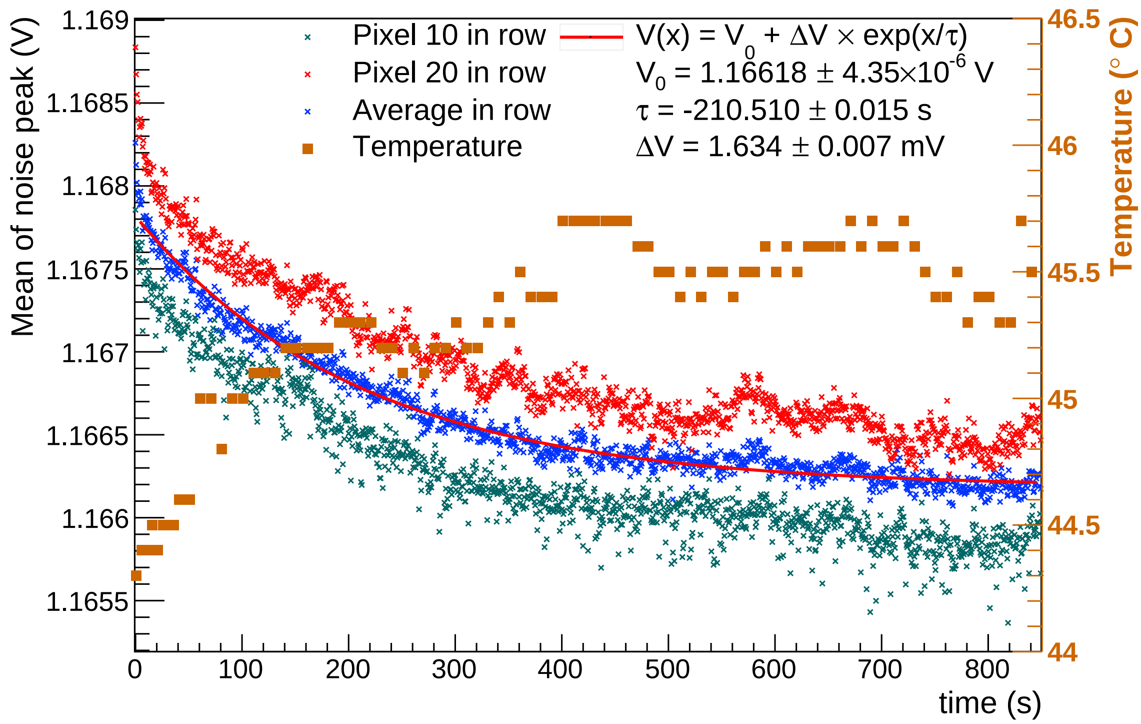

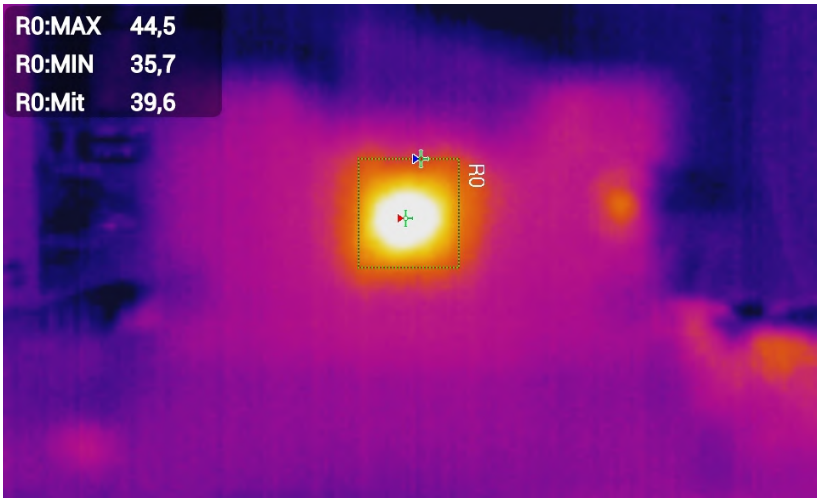

Figure 15: Heat generation of the chip. The temperature measurement over time (**top**) is taken from the maximal temperature value in the thermal image (**bottom**). The image shows a view of the daughterboard equivalent to the photo in fig. 6b. Row 0 is scanned repetitively while the chip generates heat visible through the temperature increase. The mean value of the noise peak of two example pixels together with the mean over all 64 pixels in the row are plotted and an exponential decay is fitted to the mean data. A second y-axis shows the temperature increase.

4.5. Noise peak broadening through high occupancy

One of the six bits of the tuning DACs discussed in section 4.1 defines the masking of the pixel. Figure 16 shows the successful functioning of the masking as masked strips detect no counts. During the measurement one strip is unmasked after the other and the threshold scans are shown for 1, 8, 32 and all 64 strips unmasked. A broadening of the noise peak is observed whilst unmasking more strips. Another plot demonstrates how the mean of the noise peak shifts to larger voltages as well as how its width increases. Furthermore, the shape of the noise peak changes from a symmetric Gaussian to a skewed peak. It is observed that high occupancy goes along with high digital activity within the pixel electronics as most comparators fire during a single clock cycle. From this high digital activity follows increased fluctuations on the voltage baseline. As it is these fluctuations defining the noise peak in shape and width, they cause the mean to increase by 5 mV and the standard deviation to double from 3 mV to 6 mV. It is interesting that the first unmasked strip is exposed to the same changes as the sum of all unmasked strips indicating that this effect occurs for all strips similarly. The broadening is not expected to occur under much lower occupancy when only rarely multiple pixels fire in the same clock cycle, resulting in a much less fluctuating voltage baseline. Lower occupancy is reached, when the threshold voltage is far enough from the voltage baseline so that noise fluctuations will not cause hits. Then only signals of traversing particles that deposit energy in the pixels are counted.

Altogether, DECAL threshold scans without incident radiation have been tested and understood. The tuning process aligns the single pixel noise peaks by reducing their range by a factor of 15. The chosen current setting for the pixel readout was optimized to obtain high counts. Further, a pixel reset is introduced to mitigate a voltage drift, that is sought to be eliminated in a future chip design. A repetitive scan of the same row showed that equilibrium is sufficiently approached after scanning five minutes through the pixel thresholds for heat generation. Finally, it was discussed that noise fluctuations increase when unmasking all pixels, which is not expected to effect the charge deposition of traversing particles and their hit detection.

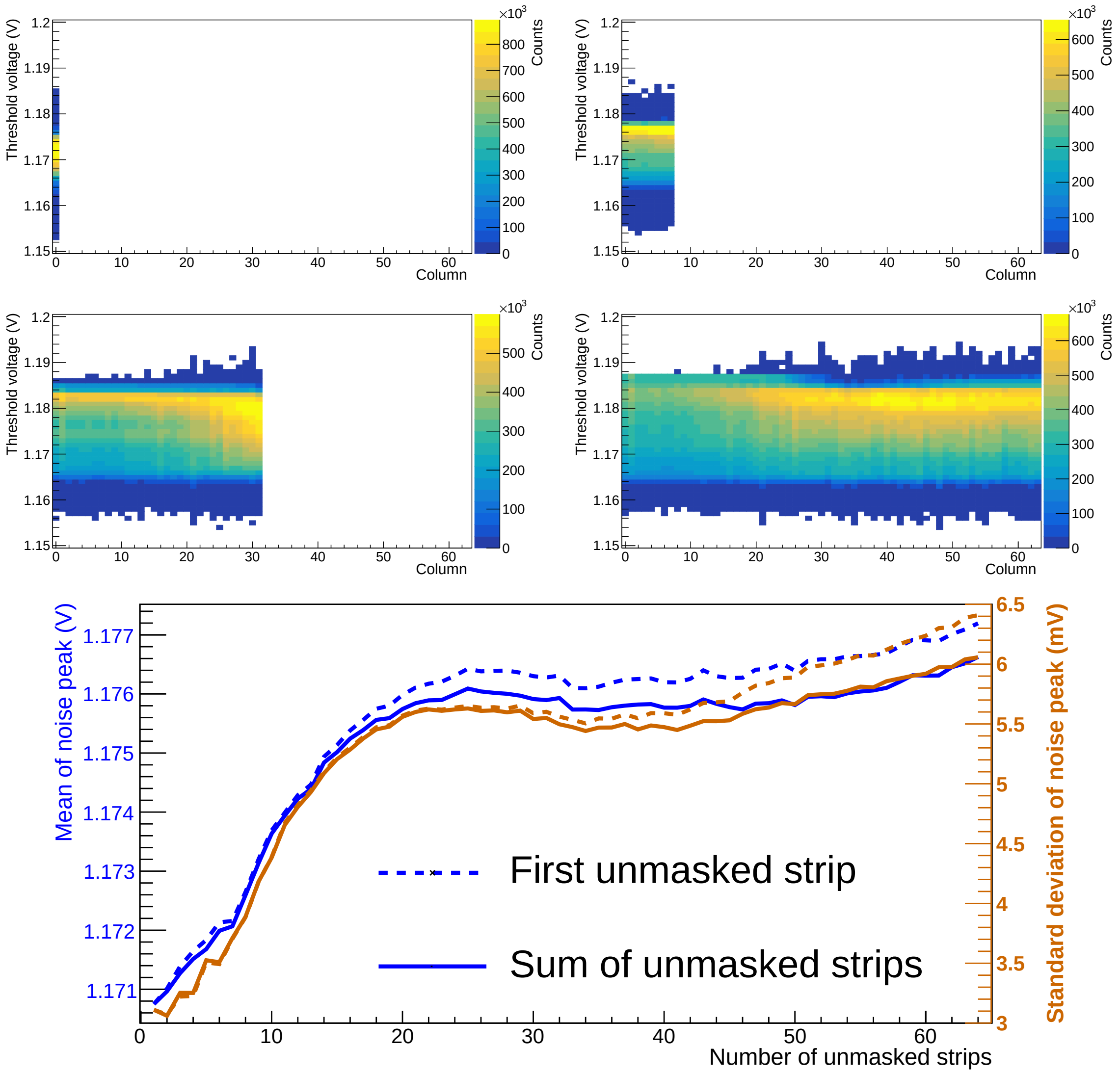

Figure 16: Mean and standard deviation of the noise peak as a function of number of unmasked strips. **Top four** plots show a threshold scan for 1, 8, 32 and 64 unmasked strips. While unmasking strips, the width and mean of the noise peak increase (**bottom**). This is the case when describing the first unmasked strip as well as the sum of all unmasked strips.

5. Signal measurements

This chapter presents signal measurements with a γ-source of americium-241 in section 5.1 and with a β-source of strontium-90 in section 5.2. The electromagnetic interaction processes of photons and electrons in silicon necessary to interpret the signal data have been outlined in section 2.1. The understanding of such signal measurements allowed us to move on to X-ray fluorescence scans, undertaken at the RAL in UK. These signal scans are discussed in section 5.3. An independent measurement of the photon fluorescence energy spectra leads to an energy calibration of the DECAL sensor and a verification of the absolute signal counts detected with the sensor. The uniformity of all DECAL pixels is investigated. Then, two different energy calibration methods are presented in sections 5.3.3 and 5.3.4 whose results come to an agreement. Moreover, the absolute DECAL counts are found to match with expectations as presented in section 5.3.5.

5.1. Americium-241 as γ-source

Americium-241 decays under α emission with a half-life of 432.6 a to excited states of neptunium-237. With 35.8 % probability a photon of 59.54 keV is emitted in the subsequent decay. A 15 MBq source at DESY Zeuthen is used and the most probable photon emissions are listed in table 1. $P_{\gamma,\mathrm{det}}$ is the photon detection probability in the 25 µm thin silicon epitax of the DECAL pixels per americium-241 decay. It calculates as the product of the photon emission probability P_γ and the absorption probability P_{ab}. Only one in around 500 photons of 59.54 keV is absorbed in the epitax. While the α particles are already absorbed by paper or very thin metal, the emitted photons will reach the detector and in the case of high energy photons even pass the sensitive region without interaction. It is noted here, that the DECAL sensor is not specifically designed to absorb and detect all photons of energies from 20 keV or higher. It is designed for the detection of secondary particles from electromagnetic shower formation when sandwiched between absorber layers.

Apart from photons, electrons are emitted that do not originate from a nuclear decay. Their energy is discrete rather than following a continuous distribution as in the case of β-particles. Instead they are Auger L-line electrons (e_{AL}) or come from internal conversion (ec), where an excited neptunium nucleus can pass its energy on to an electron in an inner shell and causing it to be emitted from the atom. A gap in the inner electron shell can consequently be filled by another electron from a higher shell under photon emission of a characteristic K or L line. Such a photon emission is also included in table 1.

5.1.1. Signal shoulder in threshold scan

A scan through threshold voltages is performed in a wide range around the background noise peak. The americium-241 source is placed as closely as possible to the sensor

Table 1: Americium-241 photon (**top**) and electron (**bottom**) emission probabilities. These emission probabilities P_γ and P_e are taken from [38]. The energy dependent photon absorption probability P_{ab} in 25 µm silicon is used to obtain the expected DECAL detection probability $P_{\gamma,det}$ for each americium-241 disintegration. The electron emission is grouped in energy intervals corresponding to the electron conversion processes. Only the internal conversion processes with $P_e > 5\%$ are listed here.

γ emission	Energy (keV)	P_γ (%)	P_{ab} (%)	$P_{\gamma,det}$ (10^{-4})
X-ray L lines (Np)	16.60	37.6	4.373	164.425
$\gamma_{2,1}$(Np)	26.34	2.40	1.188	2.851
$\gamma_{1,0}$(Np)	33.20	0.121	0.640	0.077
$\gamma_{4,2}$(Np)	43.42	0.069	0.340	0.024
$\gamma_{2,0}$(Np)	59.54	35.78	0.189	6.762
e^- emission	Energy (keV)	P_e (%)		
e_{AL}(Np)	6.04 - 13.52	36.0		
$ec_{2,1L}$(Np)	3.92 - 8.73	14.7		
$ec_{1,0L}$(Np)	10.77 - 15.58	17.3		
$ec_{4,2L}$(Np)	20.99 - 25.81	8.6		
$ec_{2,0L}$(Np)	37.11 - 37.93	31.3		
$ec_{2,0M}$(Np)	53.80 - 55.88	8.1		

in order to obtain maximal statistics. Figure 17 shows the more than 300 mV wide signal shoulder, that is described by a double error function fit. The background data is measured in absence of a radioactive source and its noise peak coincides with the main peak under source illumination. Outside this 40 mV noise range counts occur only in presence of the americium source. A turn-on behavior is detected around the mean of the error function $\mu_1 = 0.860\,\mathrm{V}$ that arises from the high energy photon emission at 59.54 keV. If no other particles would be incident, the signal shoulder is expected to stay flat after that turn-on. As listed in table 1 other photon and electron emissions happen at lower energies, that together contribute to another steep increase close to the noise peak. While absorbed photons deposit all their energy, electrons lose energy according to a broad distribution and contribute to a continuous rise covering the discrete photon emission lines. In order to speak more clearly about energy spectra the following calculation illustrates how this can be obtained from a threshold scan.

5.1.2. Energy spectrum from threshold scan

The error function used for signal fitting in the threshold scan holds the information about the signal height in the pixel electronics. A translation from the threshold scan to an energy spectrum is possible by differentiation. For this purpose, let us consider

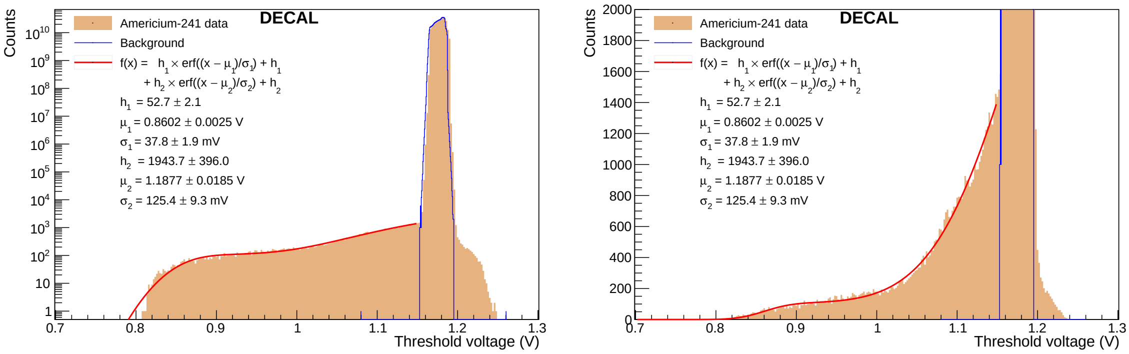

Figure 17: Threshold scan with the DECAL sensor being exposed to an americium-241 γ-source. The distribution of measured counts as a function of the threshold voltage is shown. The same data is shown on logarithmic scale (**left**) to show the signal shoulder width and the whole background noise peak (blue). The zoomed in linear scale (**right**) reveals the exact shape of the signal shoulder. A double error function is fitted to it in the region outside of the noise peak.

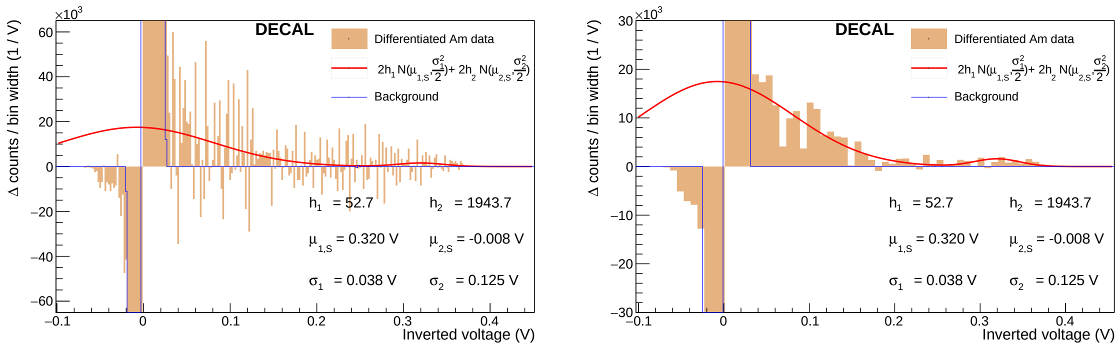

Figure 18: Numerically differentiated threshold scan and its differentiated fit function plotted on an inverted voltage axis where the mean of the background noise peak is chosen as the origin. Bin-wise data differentiation is exposed to statistical fluctuations (**left**). Additionally, the numerical differentiation is performed after combining four neighboring bins which reduces fluctuations (**right**).

the derivative of the error function

$$\frac{d}{dz}\operatorname{erf}(z) = \frac{2}{\sqrt{\pi}}e^{-z^2}. \tag{24}$$

A simple variable change is desired to account for the parameters of the function

$$z = \frac{x-\mu}{\sigma} \tag{25}$$

$$\frac{dz}{dx} = \frac{1}{\sigma} \tag{26}$$

which leads to the derivative

$$\frac{d}{dx}\operatorname{erf}\left(\frac{x-\mu}{\sigma}\right) = \frac{dz}{dx}\frac{d}{dz}\operatorname{erf}(z) = \frac{2}{\sigma\sqrt{\pi}}e^{-z^2} = \frac{2}{\sigma\sqrt{\pi}}e^{-\frac{(x-\mu)^2}{\sigma^2}}. \tag{27}$$

Abbreviation of the normal distribution

$$\mathcal{N}(\mu,\sigma^2) = \frac{1}{\sqrt{2\pi\sigma^2}}e^{-\frac{(x-\mu)^2}{2\sigma^2}} \tag{28}$$

simplifies the expression for the derivative of the error function to

$$\frac{d}{dx}\operatorname{erf}\left(\frac{x-\mu}{\sigma}\right) = 2\mathcal{N}(\mu,\frac{\sigma^2}{2}). \tag{29}$$

A threshold scan with the DECAL sensor is sensitive to the integral of the photon energy spectrum. Thus, an energy spectrum is obtained by numerical differentiation of the binned data. As derived in eq. (29) the fitted error function yields a Gaussian with narrower width parameter. Figure 18 shows a bin-wise numerical differentiation of the americium data and a differentiation where four neighbouring bins are added up to reduce statistical fluctuations. Here, the x-axis is inverted and the mean of the noise peak is chosen as the origin, so that counts at high voltages correspond to photons at high energies. Additionally, the analytically differentiated fit function is shown and still manages to describe the data. The Gaussian centered at $\mu_{1,\mathrm{S}} = 0.320\,\mathrm{V}$ describes the high energy photons emitted by americium-241 which lie at 59.54 keV. Due to the low photon absorption probability in thin silicon, this main emission line is highly suppressed by a factor of 1.89×10^{-3} (see table 1).

5.2. Strontium-90 as β-source

Strontium-90 decays via β-decay with a half-life of 28.8 a to yttrium-90 with a maximal kinetic energy of 0.546 MeV. The subsequent β-decay of ^{90}Yt with decay energy of 2.274 MeV is characterized by a half-life of 64.6 a to the stable zirconium-90 [39]. Electrons from these two decays are measured by pointing a 53 kBq source onto the DECAL sensor at a distance of about 5 mm between sensor and sealing of the source.

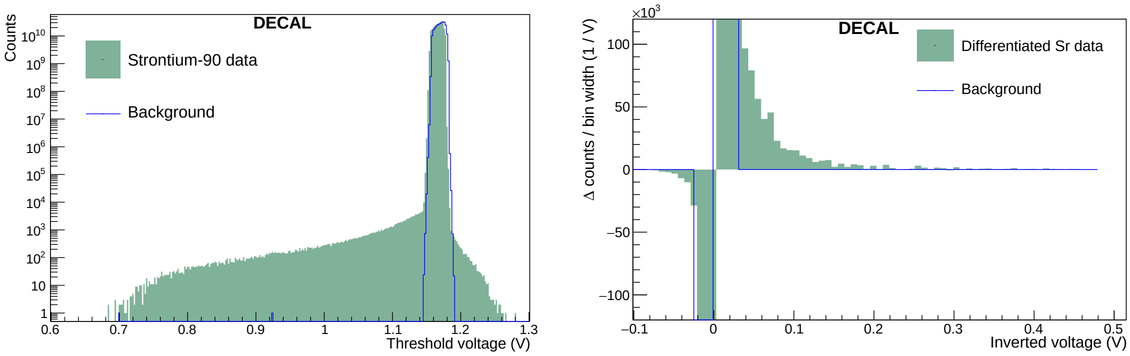

Figure 19: Threshold scan with the DECAL sensor being exposed to a strontium-90 β-source. The threshold scan is shown on logarithmic scale (**left**) to show the signal shoulder width and the whole background noise peak (blue). Its numerical differentiation (**right**) is performed after combining four neighboring bins which reduces statistical fluctuations and is plotted on an inverted voltage axis where the mean of the background noise peak is moved to the origin.

Assuming a 100% ^{90}Sr content when purchased at 2006, the source now contains 68% of strontium, 29% yttrium and 3% zirconium in terms of number of atoms. Figure 19 shows the threshold scan of DECAL under exposure of the the above described β-decays. The differentiated spectrum of four bins grouped together is plotted, too. A parametrisation or even a physically motivated fit-function is difficult to find, because several factors play into the charge deposition: Firstly, the electrons come from two different β-decays, which secondly are described by a continuous energy distribution. Additionally, each electron loses energy through ionization following a Landau straggling function. To complicate things, the energy loss is not fully deposited in the depleted silicon because secondary particles can leave it and carry away the lost energy. Nevertheless, the energy loss is estimated here through the stopping power of electrons in silicon (see fig. 2). The energy region between 0.5 and 2.5 MeV shows a rather flat behavior with a less than 10% decrease in stopping power. The mean energy loss is estimated from the stopping power S, the silicon density $\rho = 2.33\,\mathrm{g\,cm^{-3}}$ and the silicon thickness $x = 25\,\mathrm{\mu m}$ as

$$\mathrm{E_{loss}} = \rho x S = 5.825 \times 10^{-3}\,\mathrm{g\,cm^{-2}} \times S. \tag{30}$$

In this estimation, S is assumed to stay constant while the traversing electron loses energy. Actually, S is energy dependent as described by fig. 2. At an electron energy of 1.0 MeV the mean energy loss evaluates to

$$\mathrm{E_{loss}}(S = 1.51\,\mathrm{MeV\,cm^2\,g^{-1}}) = 87.96\,\mathrm{keV}. \tag{31}$$

Assuming that the full energy loss is deposited at the edge of the signal shoulder, a maximal signal height is observed of

$$\mathrm{V_{Sr90}} = 488\,\mathrm{mV}. \tag{32}$$

This value can be read from the differentiated spectrum as the entry highest in voltage compared to the mean of the background noise peak. The number of created electron-hole pairs through ionization is obtained from the creation energy of $\epsilon = 3.6\,\mathrm{eV}$ as $87.96\,\mathrm{keV}/\epsilon = 24433$ and yields a conversion gain of

$$\mathrm{c_{g,Sr90}} = \frac{\mathrm{V_{Sr90}}}{24433} = 19.97\,\mathrm{\mu V/e^-}. \tag{33}$$

For the future, a trigger setup is proposed for physical understanding of the whole strontium spectrum by selecting only high energy electrons, that act as MIPs: A setup using two scintillators or an absorber and a scintillator behind the DECAL sensor allows to trigger on the high energy electrons that deposit energy through ionization in the DECAL silicon epitax and have enough energy to reach the trigger system. An interesting question is whether the triggered spectrum exhibits a local maximum characteristic for the most probable value (MPV) of a Landau distribution.

5.3. X-ray source

In the following section threshold scans of an X-ray fluorescence source are discussed. The used X-ray tube facility is located at the Technology Department of RAL, UK and accelerates electrons onto a tungsten target. The emitted photons follow a continuous bremsstrahlung spectrum with tungsten excitation lines. These primary photons hit an exchangeable target and excite its K and L lines, mainly. Subsequent de-excitation occurs under isotropic photon emission, leading to a peaked energy spectrum with much reduced bremsstrahlung background compared to the spectrum of the primary photons.

First, the photon energy spectra of six different target materials - namely Cd, Cu, Fe, Mo, Pb and W - measured with the High energy X-ray imaging technology (HEXITEC) detector are presented. Secondly, the uniformity of the DECAL pixels is proven in both row and column dimension. The spectra of individual pixels within one row are compared as well as the spectra of different rows. This motivates the summation of all pixel counts used to obtain high statistics for the DECAL energy spectra of all target materials in figs. 24 and 25. Based on this spectral data two independent energy calibration methods are developed that agree with each other (sections 5.3.3 and 5.3.4). Finally, the estimation of absolute counts is validated through measurements in section 5.3.5.

Table 2: HEXITEC energy calibration. For each target material the significant nominal fluorescence peak energies are presented as decimal point numbers in unit keV [41]. The peak positions identified through the HEXITEC detector are listed with their bin value (integer in bracket). Only those energies with a corresponding bin value enter the linear energy calibration shown in fig. 20.

target	$K_{\alpha1}$	$K_{\beta1}$	target	$L_{\alpha1}$	$L_{\beta1}$	$L_{\gamma1}$
Fe	6.40	7.06	W	8.40	9.67	11.28
				(255)	(300)	(360)
Cu	8.05	8.91	Pb	10.55	12.61	14.76
	(260)			(345)	(420)	(490)
Mo	17.48	19.61				
	(590)	(665)				
Cd	23.17	26.10				
	(790)	(900)				

5.3.1. Photon energy spectra of target materials with HEXITEC

The High Energy X-ray Imaging Technology (HEXITEC) is a 80 x 80 Cadmium telluride (CdTe) pixel detector with an overall sensitive area of 4 cm^2 developed and manufactured at RAL [40]. Due to the high photon absorption probability of CdTe and its relatively thick 1 mm pixels it detects all photons up to 200 keV starting from a cut-off energy at 4 keV. The HEXITEC detector is used to measure the energy spectrum every time before placing the DECAL sensor at the same position. The HEXITEC energy calibration in fig. 20 is performed by identifying the characteristic K_α, K_β and K_γ peaks and thus translating the x-axis from bins to energy. The corresponding bin values and peak energies that enter the energy calibration are listed in table 2 and are independent of the charge sharing correction mode, that can be selected. Charge sharing can be compensated by either adding the signals of neighboring pixels or selecting only those charge depositions where neighboring pixels do not detect a charge. The mode of addition is chosen for this analysis because it offers higher statistics as no charge deposition is dismissed. Qualitatively it has one implication that for the copper spectrum a smaller second peak is formed at double the bin value of the main peak, because coinciding neighboring charge depositions are summed up, too. While the HEXITEC detector is expected to absorb all photons up to 200 keV this is not the case for the DECAL sensor. Its 25 µm epitaxial silicon has a suppressed absorption probability because of its thin sensitive region and the use of silicon essential for monolithic sensors rather than CdTe. The material dependence has been shown in fig. 3a. In order to account for this effect, the HEXITEC energy spectra are corrected by the energy dependent absorption probability of photons, as shown in fig. 21. While the overall copper counts are suppressed by a factor of 3.2, the cadmium spectrum suffers from suppression by 22.6 as it peaks at higher energies.

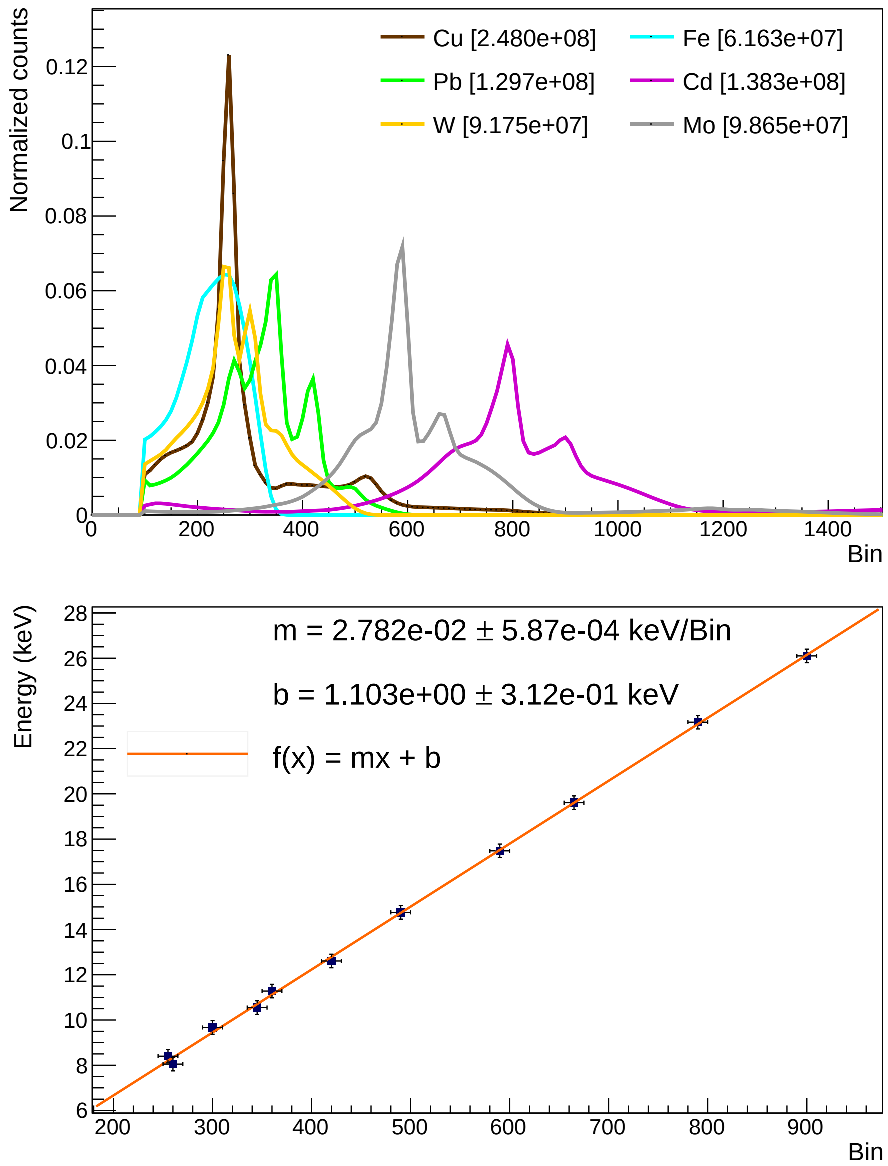

Figure 20: HEXITEC energy spectra (**top**) for all six X-ray target materials. The normalization constants are stated in the legend. The energy calibration (**bottom**) translates from bin to energy and uses the excitation energies from [41] that are listed in table 2.

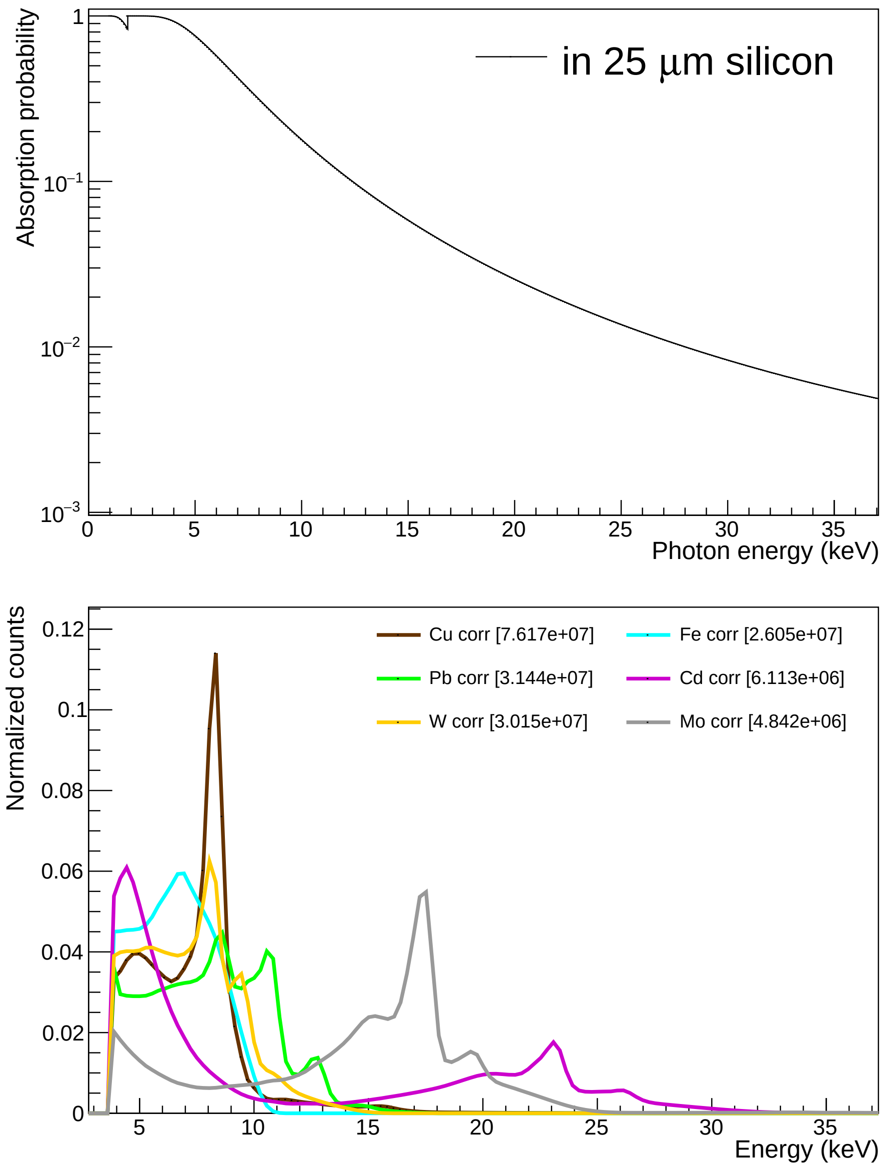

Figure 21: The energy dependent absorption probability in 25 µm silicon (**top**) is taken into account for the HEXITEC energy spectra. The spectra are corrected (**bottom**) to enable the comparison with the DECAL data. The simultaneously detected charge of neighboring pixels is added up in order to account for charge sharing. Normalization constants of the spectra are stated in the legend.

5.3.2. Pixel- and row-wise DECAL uniformity

The tuning procedure of section 4.1 aligns the voltage baselines of the pixels based on measurements of the noise peak. It is investigated here whether the individual pixels within one row behave uniformly with regards to signal height formation from X-ray absorption. The clear copper fluorescence peak is designated to compare the threshold scan of these pixels. A double s-curve fit is performed to the threshold scans of individual pixels in row 32. The three fit parameters describing the main copper peak with the error from the fit are plotted over the row index in fig. 22. Despite the low statistics all pixels are sensitive to the signal shoulder and describe it with similar parameters. For comparison, a horizontal line represents the fit parameter obtained when summing the row data among all pixels. Its spectrum is shown on logarithmic and linear scale in fig. 29. The fluctuation of the mean positions μ_1 from the single pixel fits is quantified with a standard deviation of only 1.5 mV, showing that the signal turn-on occurs at similar threshold voltages. What is more, the absolute counts measured - estimated by the height parameter - speak for an independent and uniform signal counting. For the mean of 83.7 a Poisson distribution has a width of 9.1, the square root of the mean. This width slightly exceeds the standard deviation of 7.0 of the h_1 sample simply through the statistical nature of Poisson counting. Consequently, the signal shoulders are described by similar parameters in each pixel. The expectation that the tuning of noise peaks aligns the whole signal shoulders turns out to be correct, which motivates the summation of the pixel counts within one row.

Similarly, the uniformity between rows is investigated by comparing the signal shoulders of 7 different rows, namely 2,12,22,32,42,52 and 62. They are covering the whole sensor in equal steps. A double s-curve is fitted to the threshold scans of these seven rows and the parameters describing the copper fluorescence peak are plotted in fig. 23 over their row index. The standard deviation of the sample of the seven height parameters exceeds the expectation of a Poisson statistics. This is due to the fact that two different height values are favoured, around 540 and 615. The behaviour can be well explained by the row measurements arising from different measurement runs. While rows 2, 12 and 32 were measured at one day, the other four rows were scanned the next day. The turn-off and restart of the X-ray tube is the most likely explanation for a lower photon flux hitting the DECAL sensor on the second day. This is supported by an additional high statistics measurement of row 32 indicated by the horizontal line. It was performed on the second day and agrees with the other rows scanned on the same day. It is noted that within the two groups, all heights agree with each other within the statistical error from the fit. The parameters μ_1 and σ_1 are independent of the flux and show good agreement among the seven rows with a low standard deviation of 0.4 and 0.3 mV respectively. In comparison to the single pixel fits described above the whole row fits presented here result in an around four times lower standard deviation on μ_1 and σ_1 as the statistics is higher when summing counts over an entire row. This supports the assumption that fluctuations in the fit parameters are only of a statistical nature and motivates the summation of all pixel counts over the whole chip geometry.

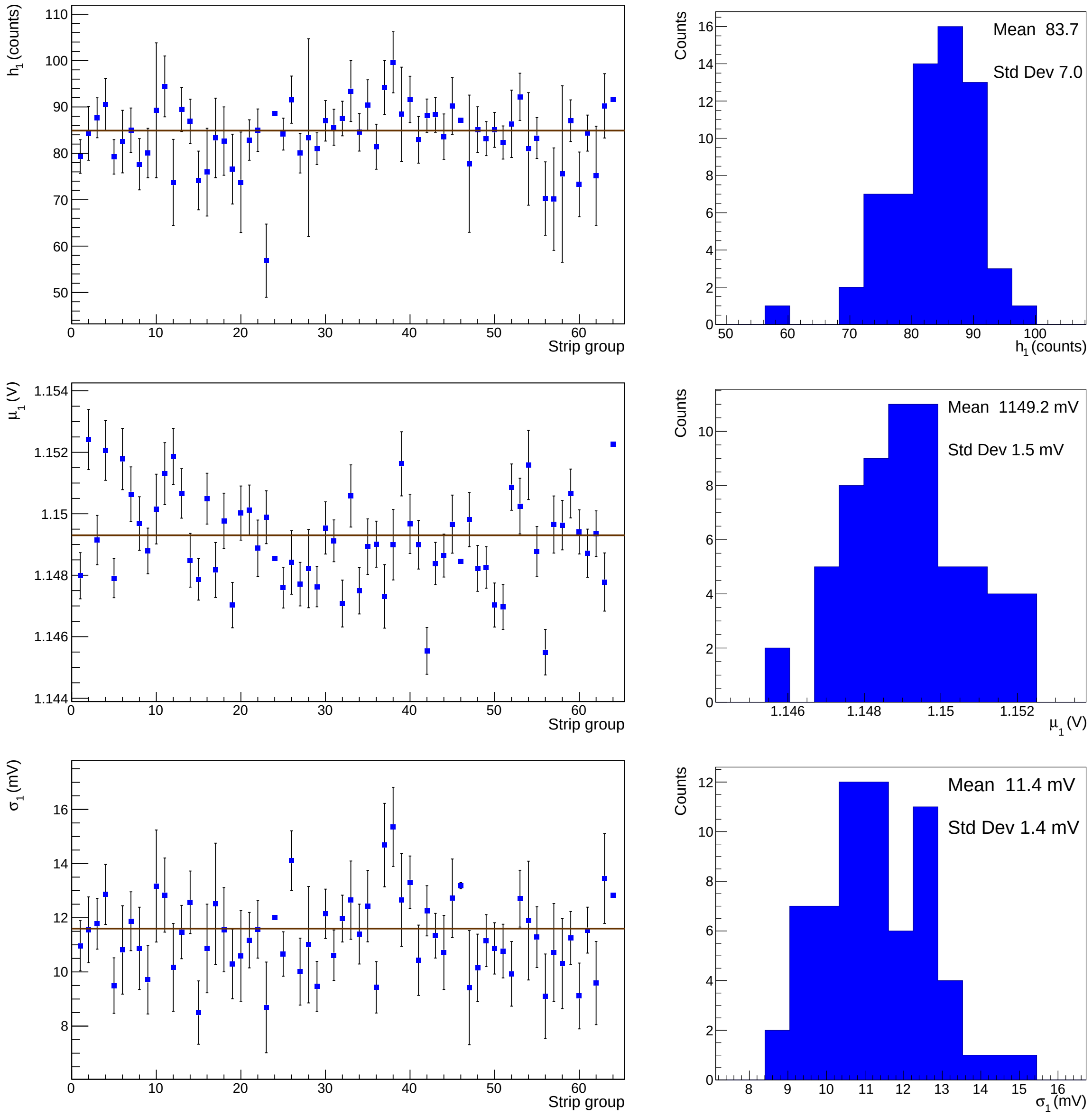

Figure 22: Pixel uniformity within one row. The three fitting parameters height h_1 (**top**), mean μ_1 (**middle**) and width σ_1 (**bottom**) of an s-curve fit are plotted over the row index (left) and are histogrammed (right). The s-curve describes the main copper fluorescence peak and is fitted to the data of individual pixels. The horizontal lines represent the fit parameters obtained from fitting to the sum of all pixel counts and in the case of h_1 scaled down by a factor of 64.

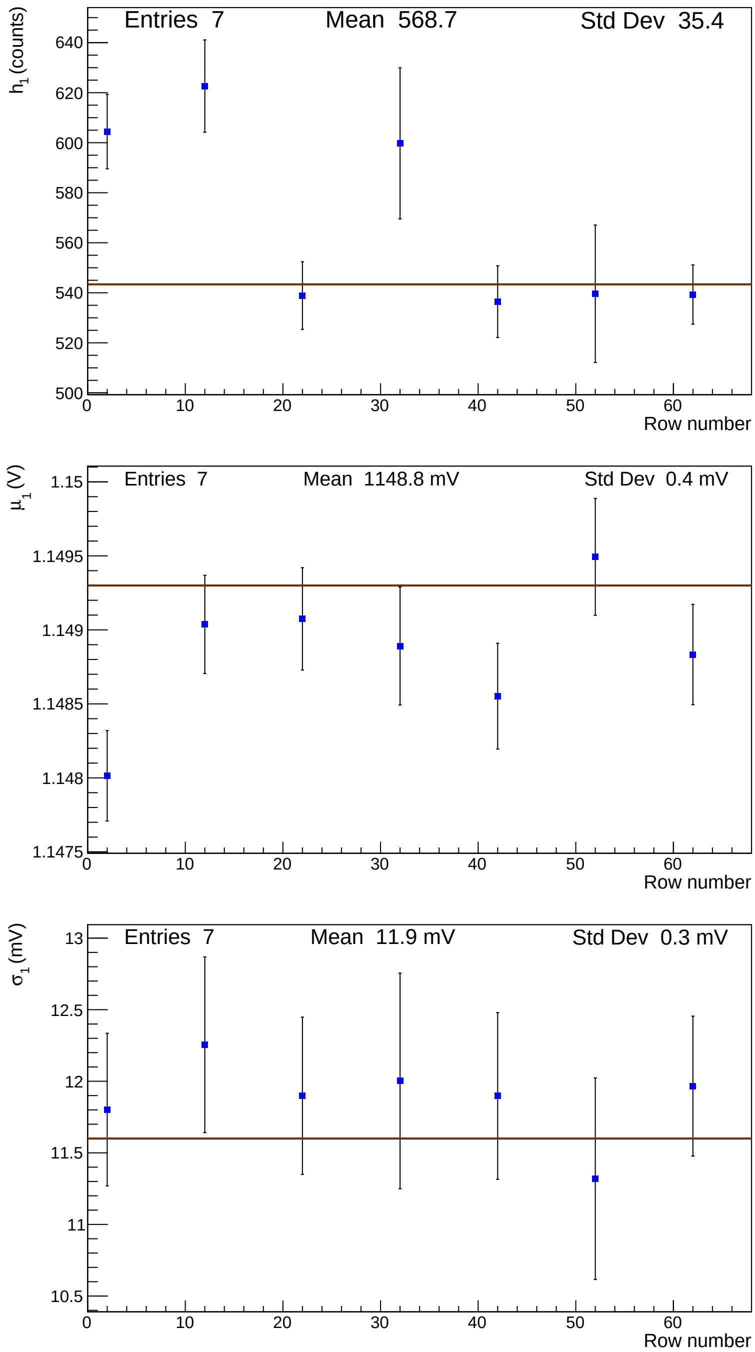

Figure 23: Pixel uniformity among seven different rows. A double s-curve is fitted to the threshold scans of seven different rows. The three fitting parameters height h_1 (**top**), mean μ_1 (**middle**) and width σ_1 (**bottom**) of the s-curve describing the main copper fluorescence peak are presented here. Error bars represent the uncertainty on the fit parameters. The horizontal line indicates the fit parameters of a repeat scan of row 32 with 10 times higher statistics where h_1 is scaled down accordingly by a factor of 10.

5.3.3. DECAL energy calibration through X-ray peak energies

A DECAL energy calibration is needed to translate the voltage signal heights of the DECAL sensor to an energy scale. The straightforward way to do so is to compare the peak position in the differentiated DECAL spectra with the nominal X-ray peak energies. For all six X-ray fluorescence targets threshold scans have been performed for one row and all rows enabled. These scans are shown in figs. 29 to 31 on logarithmic and linear scale. DECAL energy spectra are obtained through differentiation as described in section 5.1.2 and presented in figs. 24 and 25 together with the differentiated fit functions. The parameter μ_S is the mean of the Gaussian and describes the peak position obtained from the DECAL spectra. This values is compared to the nominal X-ray peak energies in fig. 26. The americium measurement is also included to cover a wider energy range. An absolute uncertainty of 1 keV on the peak energies is assumed as this is the energy resolution of HEXITEC. While the fluorescence energy peak positions are known with much better precision, only the HEXITEC data verifies the excitation of the correct energy levels. The error on the signal height μ_S is the corresponding width of the Gaussian peaks in the DECAL energy spectra. The calibration procedure is compatible with a linear model and motivates the assumption of an approximately linear response over the energy range up to 60 keV. The signal height per keV is obtained through the gradient

$$m = 5.51 \pm 0.52\,\mathrm{mV/keV}. \tag{34}$$

A limitation of this procedure is that data points are only taken at the peak positins, while the full spectral data of DECAL and HEXITEC are not considered. As a consequence, the whole energy range is not covered in equidistant energy steps which would be preferred for an energy calibration. In the future the data points can be appended through fluorescence measurements of other target materials or radioactive sources such as the decay of cadmium-109.

5.3.4. DECAL energy calibration through HEXITEC energy spectra

More sophisticated is the usage of the HEXITEC energy spectra to calibrate DECAL. This procedure takes the full energy range of the spectra into account rather than just the main peak positions as in section 5.3.3. Figure 27 shows again the differentiated DECAL threshold scans for the whole chip being enabled. Here, the HEXITEC energy spectra are fitted with a normalization constant C as well as a multiplicative constant a for the x-axis translation. This way a signal voltage V is obtained from a photon of energy E as

$$\mathrm{V} = a\mathrm{E}. \tag{35}$$

For each X-ray target three different fits are performed with the above parameters. The blue dashed line takes the uncorrected HEXITEC spectrum for each material as the shape for the fit. The dashed black line represents the corrected spectrum, that takes the absorption probability in 25 µm silicon into account. The red line includes the same correction and is additionally smeared by a Gaussian convolution. The width of the

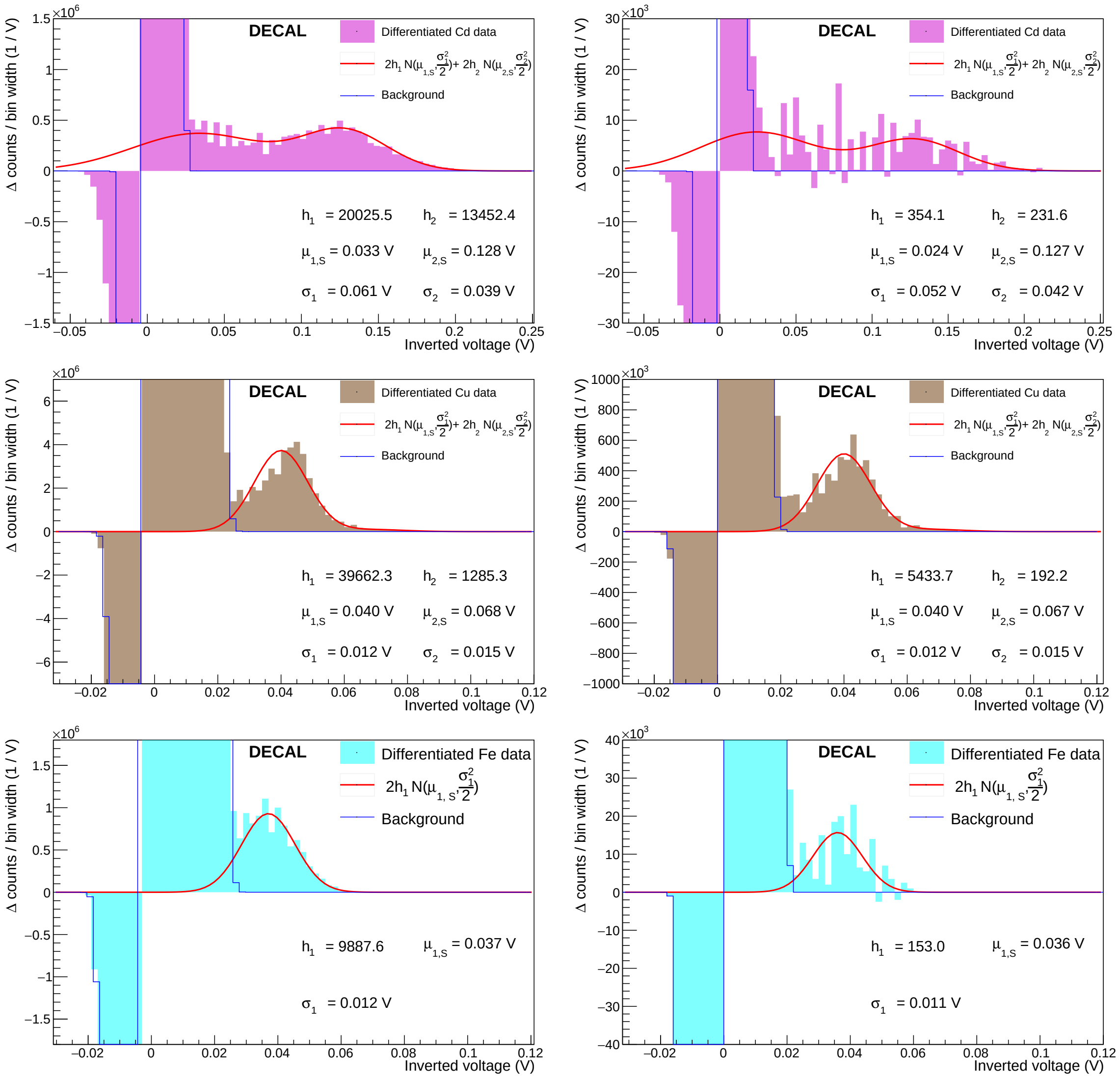

Figure 24: Differentiated DECAL threshold scans under X-ray fluorescence of target materials Cd (**top**), Cu (**middle**) and Fe (**bottom**). Left plots show data for the whole chip enabled, while the right data arise from only row 32 being unmasked. The red line is the numerically differentiated fit function and the blue represents a background measurement with the X-ray machine turned off.

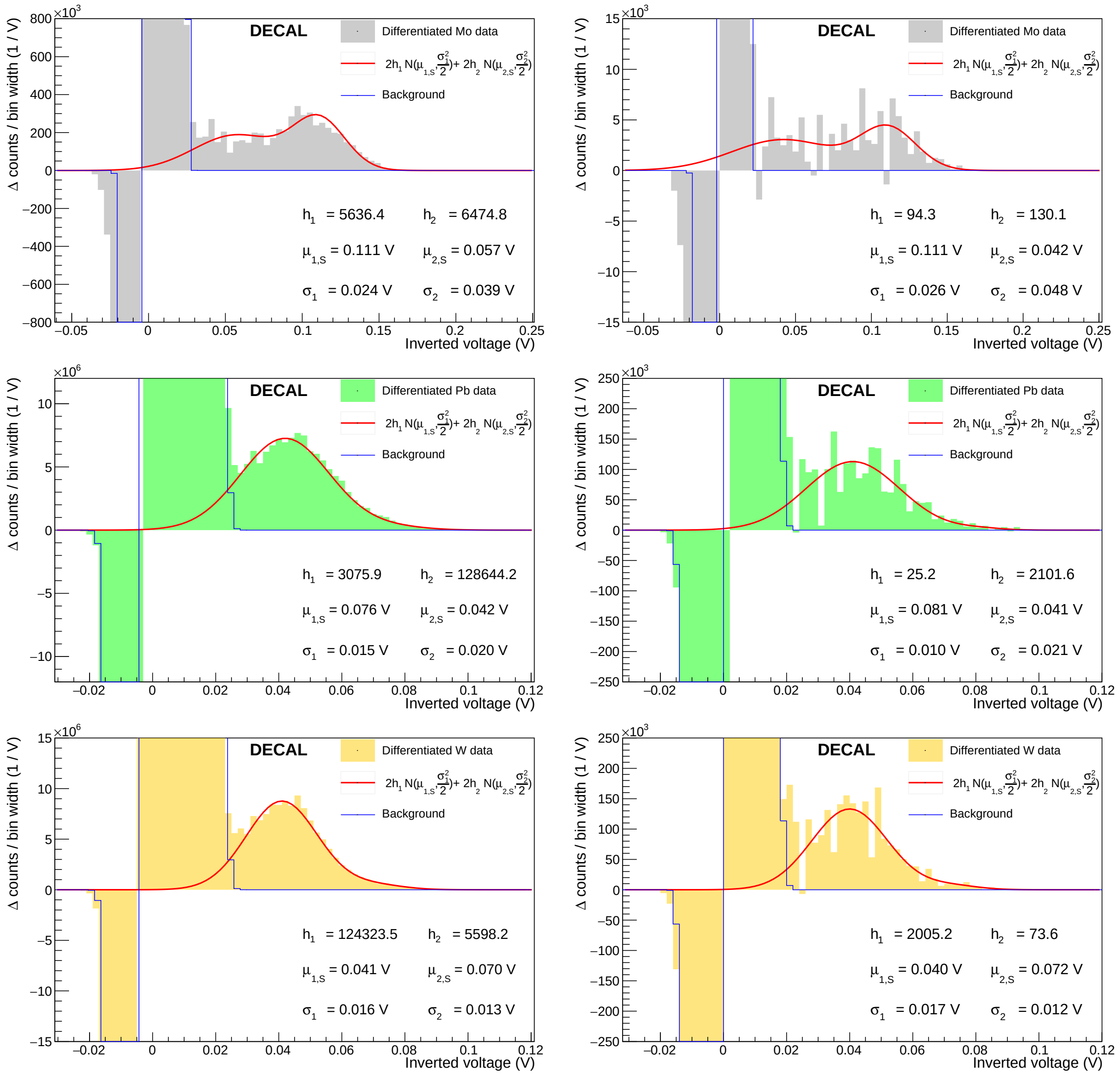

Figure 25: Differentiated DECAL threshold scans under X-ray fluorescence of target materials Mo (**top**), Pb (**middle**) and W (**bottom**). Left plots show data for the whole chip enabled, while the right data arise from only row 32 being unmasked. The red line is the numerically differentiated fit function and the blue represents a background measurement with the X-ray machine turned off

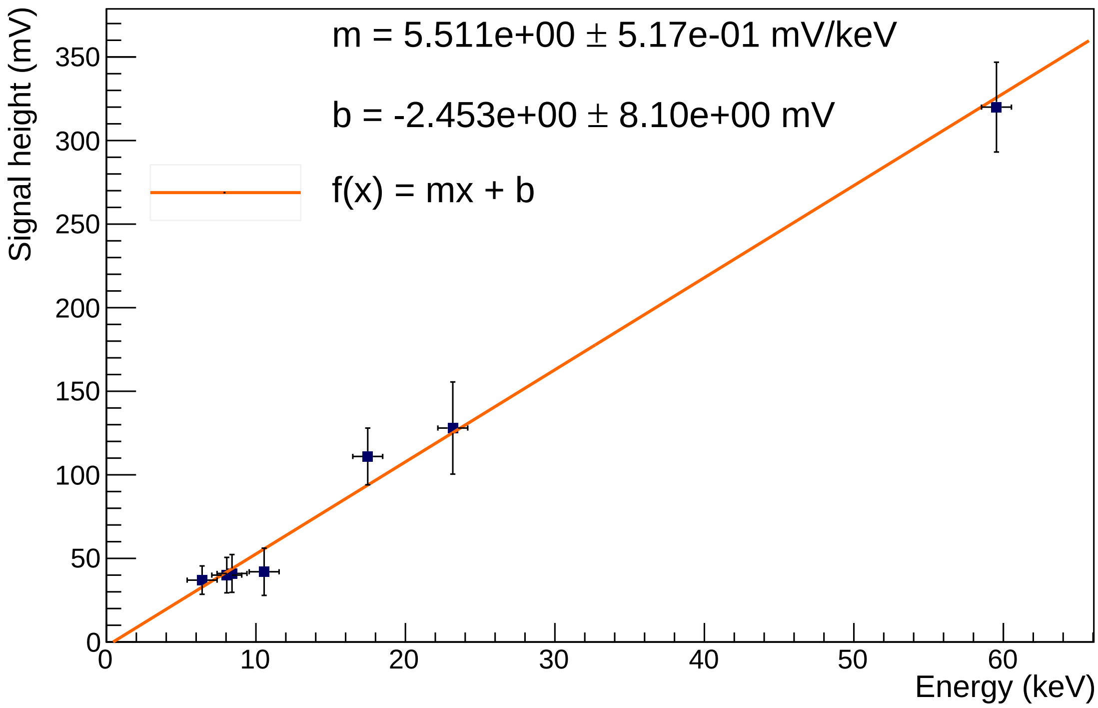

Figure 26: DECAL energy calibration by peak positions. The mean value μ_S from the differentiated spectra in figs. 18, 24 and 25 is plotted over the nominal X-ray peak energy for each target material. The uncertainty on the signal height is the width of the Gaussian peaks and the energy uncertainty is assumed to be 1 keV, the full width at half maximum of the HEXITEC peaks.

Table 3: DECAL signal height, energy resolution and conversion gain obtained from fitting the HEXITEC spectral shape to DECAL energy spectra. The DECAL chip is exposed to X-ray fluorescence from six different target materials that emit photons close to their characteristic peak energies E_{peak}. The conversion gain is obtained by assuming one electron-hole pair produced for every 3.6 eV of photon energy.

target material	E_{peak} (keV)	signal height a (mV/keV)	conversion gain c_g (µV/e^-)	energy resolution σ_E (keV)
Fe	6.40	5.26	18.93	0.82
Cu	8.05	5.46	19.66	0.80
W	8.40	5.67	20.41	0.88
Pb	10.55	5.05	18.19	1.92
Mo	17.48	6.08	21.92	1.57
Cd	23.17	5.74	20.78	3.06

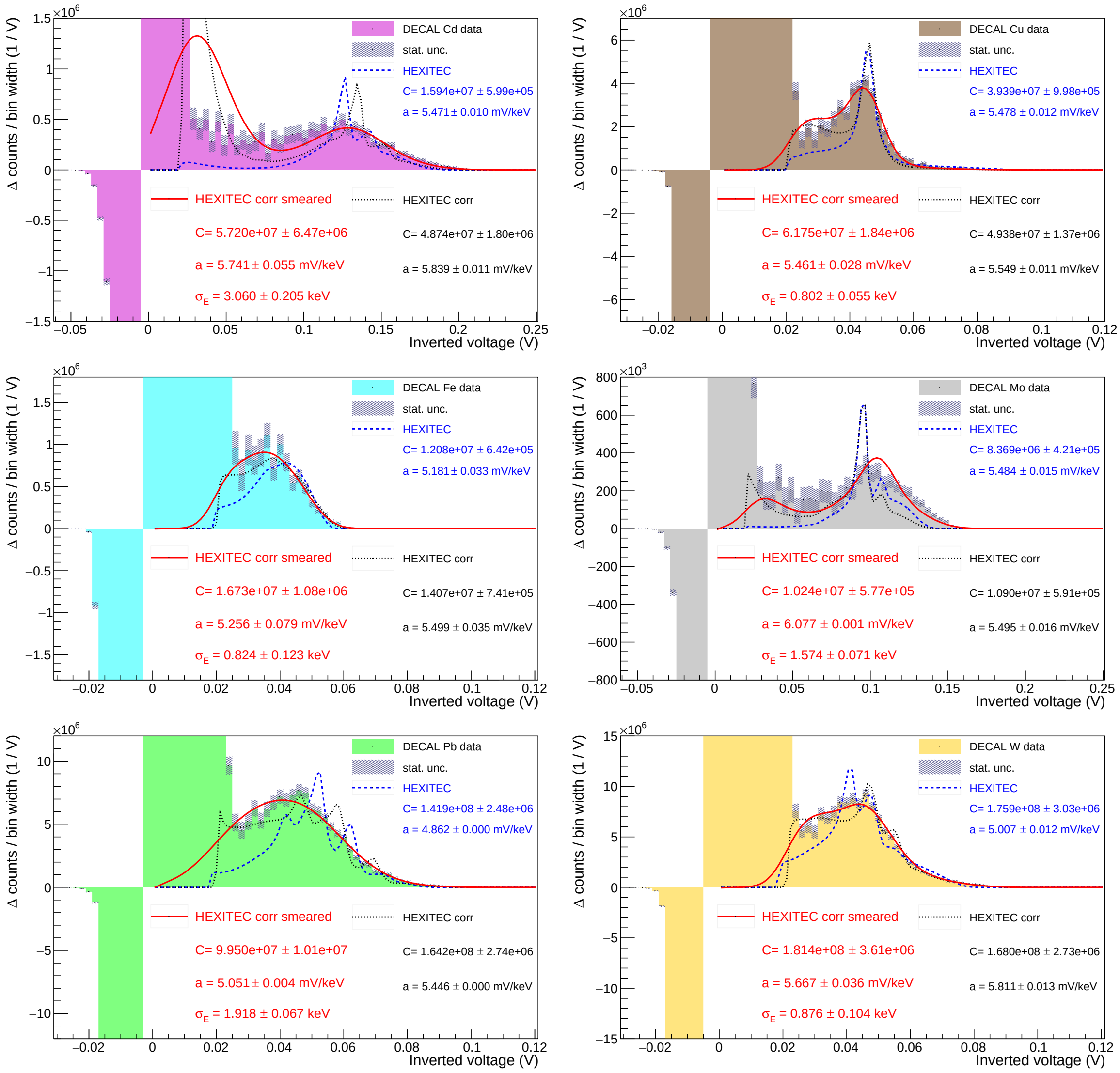

Figure 27: HEXITEC energy spectra fitted to differentiated DECAL threshold scan data under X-ray fluorescence. For all six X-ray target materials the uncorrected HEXITEC energy spectra (dashed blue) and the corrected ones (dashed black) are fitted. The spectra are scaled with a normalization constant C and multiplied in the voltage range by a factor a to translate from energy to voltage, according to eq. (35). The corrected red curve has an additional fit parameter σ_{E}, that is the width when smeared with a Gaussian convolution. The statistical uncertainties (dashed area) are propagated from the bin entries of the threshold scans from which the differentiation is performed.

smearing is defined by the fit parameter σ_E. The uncorrected and corrected spectra for all six X-ray targets have already been shown in fig. 21. Notably, the correction for the absorption probability in 25 µm silicon describes the DECAL data over the voltage range including the range close to the noise peak that corresponds to low photon energies. Further, the Gaussian smearing is needed to broaden the narrow HEXITEC peaks. The explanation for the smearing of DECAL peaks is manifold. The differentiated DECAL spectrum is not directly measured as counts as in the case of HEXITEC but obtained through differentiation of the measured counts (see section 5.1.2). This leads to a larger propagated uncertainty on the bin entries, that exceeds the one of a Poisson-like counting and is thus more prone to fluctuations. As a consequence, higher statistics must be obtained to receive a clear energy spectrum. Also, the sensitive measurement time of DECAL for the shown scans lies between 2.5 and 12.5 s per bin entry (see t_D in table 4) while each HEXITEC measurement lasted 600 s. t_D is set comparatively low, because the threshold voltage is varied in steps of 2 mV and t_D is the time that DECAL is sensitive for each of these steps. Most importantly, σ_E contains the intrinsic energy resolution of the DECAL pixels including its integrated readout and can be understood as an upper bound for it. Larger measurement times and smaller threshold voltage steps are expected to reduce the statistical contribution.

The obtained energy resolution σ_E and the signal height a are collocated in table 3 and sorted by the characteristic fluorescence peak energies E_{peak} of the target materials. The mean and standard deviation of the signal height for the six result sample quantifies the signal voltage height per keV of absorbed photon energy as

$$a = 5.54 \pm 0.37\,\text{mV/keV}. \tag{36}$$

It is in good agreement with the gradient $m = 5.51 \pm 0.52\,\text{mV/keV}$ obtained in fig. 26 through the energy calibration by peak positions. This agreement is important to substantiate the claim of a linear dependence of signal height and photon energy up to an energy of 60 keV as the americium measurement enters the determination of m but not of a. A 30% reduction on the uncertainty of a compared to m is achieved by including all spectral data and it is noted, that the nominal X-ray peak energies do not enter its calculation because HEXITEC is used for reference. This calibration procedure is especially useful when the X-ray spectra are not highly peaked at the characteristic energies but form multiple peaks or a broader spectrum. As another result, the conversion gain is proportional to a, when expressing each keV of photon energy as the number of electron-hole pairs produced. From the production energy of $\epsilon = 3.6\,\text{eV}$ for each pair the average conversion gain of

$$c_g = 19.95 \pm 1.32\,\mu\text{V/e}^- \tag{37}$$

is found. This is in good agreement with the conversion gain of $20\,\mu\text{V/e}^-$ already published in [29] and the gain obtained through electrons from the strontium-90 source that was found to be $19.97\,\mu\text{V/e}^-$. The uncertainty estimation presented here is feasible

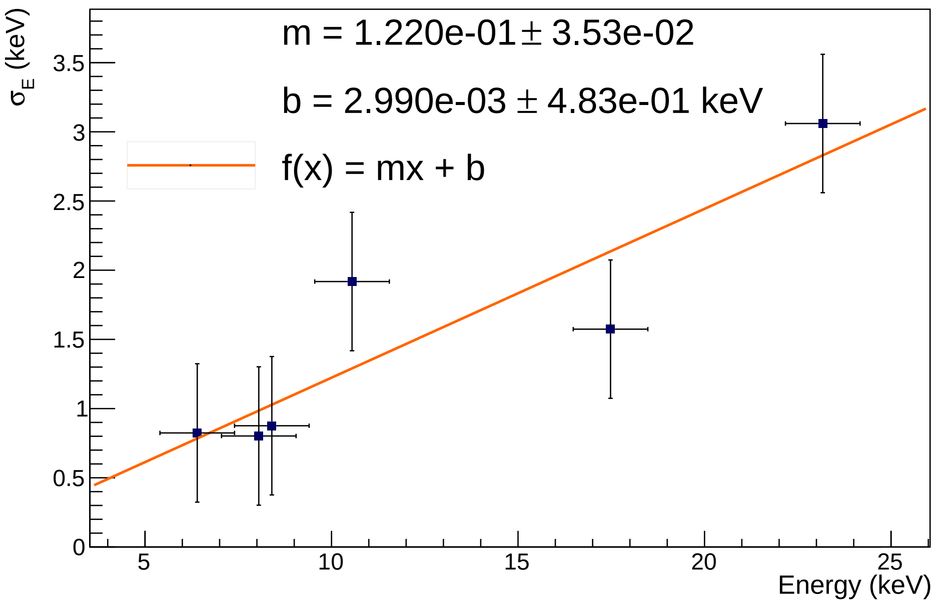

Figure 28: DECAL energy resolution as a function of the photon energy. The parameters σ_{E} describing the energy resolution in the spectral fits from fig. 27 are plotted over the characteristic X-ray fluorescence energy. HEXITEC's full width at half maximum being 1 keV this is assumed to be the uncertainty on the fluorescence energy and half of it the uncertainty on the energy resolution of each data point.

by including the analysis of all six X-ray targets which then permits better precision on the conversion gain.

For the energy resolution σ_{E} an increase with energy is observed, that is compatible with a linear model. Figure 28 finds a relative energy resolution of

$$\frac{\sigma_{\mathrm{E}}}{\mathrm{E}} = 12.2 \pm 3.5\% \tag{38}$$

and is obtained and presented for the first time for DECAL. The data point that lies above the linear model is the Gaussian smearing of the Pb spectrum. It is not expected to be very sensitive to the smearing parameter, because it is already broad before the smearing as illustrated by the dashed black line in fig. 27. It is noted again, that σ_{E} is considered to be the upper bound for the intrinsic DECAL energy resolution, because higher statistics are expected to decrease this parameter.

5.3.5. Expected and measured counts

The previous sections lead to an understanding of the peak positions in the DECAL threshold scans and its differentiation. This allows an energy calibration, mapping signal voltage height to photon energy. Another important analysis is to compare the absolute number of measured counts with expectations. The correction of the HEXITEC energy spectra by the photon absorption probability in fig. 21 enables the estimation of the measured DECAL counts. The normalization constants $\mathrm{C_H}$ of the corrected spectra are obtained during a measurement time of $\mathrm{t_H} = 600\,\mathrm{s}$ and can be compared to the signal shoulder height of the DECAL threshold scans. For that the sensitive area of HEXITEC, $\mathrm{A_H} = 400\,\mathrm{mm}^2$, and of DECAL, $\mathrm{A_D} = 12.39\,\mathrm{mm}^2$, are taken into account as well as the DECAL measurement time $\mathrm{t_D}$ for each threshold step. Further, the X-ray tube current is raised between HEXITEC and DECAL measurements from $\mathrm{I_1}$ to $\mathrm{I_2}$ to provide sufficient DECAL counts and avoid the saturation of HEXITEC which runs at a readout frequency of 1.591 kHz. The photon production rate is expected to be proportional to the X-ray tube current, thus the amplification factor $\mathrm{a_I} = \mathrm{I_2}/\mathrm{I_1}$ is introduced. All parameters are summarized in table 4 that enter the calculation of the expected DECAL counts

$$\mathrm{C_e} = \mathrm{C_H}\frac{\mathrm{A_D}}{\mathrm{A_H}}\frac{\mathrm{t_D}}{\mathrm{t_H}}\mathrm{a_I} \tag{39}$$

$$= \mathrm{C_H t_D a_I} \cdot 5.163 \times 10^{-5}\,\mathrm{s}^{-1}. \tag{40}$$

Constant parameters are already substituted. The expectation in scan type "Row" is further scaled down by a factor of 1/64, because only this fraction of the sensor area is enabled. For comparison, the measured DECAL counts $\mathrm{C_m}$ are calculated from the error function fits to the threshold scans, that are all shown in figs. 29 to 31. Due to the 4 keV cut-off after which HEXITEC is sensitive, the fit functions are evaluated at a corresponding distance below the mean of the DECAL noise peak. According to the the first DECAL energy calibration in fig. 26 the photon energy of 4 keV corresponds to a signal height of 19.59 mV, making it the separation from the noise peak mean.

Having the measured DECAL counts $\mathrm{C_m}$ and the expected ones $\mathrm{C_e}$ at hand, their ratio is calculated and presented in table 5. The uncertainty on the ratio is mainly determined by the uncertainty on the HEXITEC counts $\mathrm{C_H}$. The comparison of the different charge sharing modes in the HEXITEC software shows differences of up to 20% in the overall counts, motivating this as a relative uncertainty on $\mathrm{C_H}$. Another source of uncertainty is that the currents for the primary electron source $\mathrm{I_1}$ and $\mathrm{I_2}$ can be set with 0.1 mA precision. As a contribution from the DECAL threshold scan, the uncertainty on the measured counts in each threshold step is assumed to be the square root of counts, inherent for a Poisson counting process. All above sources of uncertainty contributions are propagated through the calculation of the ratio $\mathrm{C_m}$ to $\mathrm{C_e}$. Other sources are negligible as the timing through the clock cycles of the electronics is assumed to be precise, such as the area of the sensors. Except for molybdenum - all

Table 4: Expected DECAL counts. The sensitive area of HEXITEC is $A_H = 400\,mm^2$ and the one of DECAL is $A_D = 12.39\,mm^2$. In scan type "Row" only one row is unmasked so the active chip area is reduced by a factor of 64. a_I is the amplification factor due to a current increase in the X-ray tube from I_1 to I_2 between HEXITEC and DECAL measurements. The HEXITEC counts C_H are the corrected normalization constants from fig. 21 obtained during the 600 s measurement time. The measurement time of each DECAL threshold step is stated as t_D. The expected DECAL counts C_e are calculated according to eq. (40).

target material	Scan type	I_1 (mA)	I_2 (mA)	a_I	C_H (10^5 counts)	t_D (s)	C_e (counts)
Cd	Row	1.5	29.0	19.33	61.1	6.25	596
Cd	Chip	1.5	29.0	19.33	61.1	6.25	38 134
Cu	Row	1.0	10.0	10.00	761.7	25.0	15 361
Cu	Chip	1.0	10.0	10.00	761.7	2.5	98 310
Fe	Row	10.2	10.2	1.00	260.5	12.5	263
Fe	Chip	10.2	10.2	1.00	260.5	12.5	16 811
Mo	Row	7.0	26.0	3.71	48.4	12.5	181
Mo	Chip	7.0	26.0	3.71	48.4	12.5	11 606
Pb	Row	1.0	10.0	10.00	314.4	12.5	3170
Pb	Chip	1.0	10.0	10.00	314.4	12.5	202 893
W	Row	1.5	16.0	10.67	301.5	12.5	3243
W	Chip	1.5	16.0	10.67	301.5	12.5	207 539

Table 5: Comparison of expected C_e and measured C_m DECAL counts. The expectation is calculated in table 4 via eq. (40). The measured DECAL counts C_m are obtained from the fitting parameters of the counts 19.6 mV below the mean of the noise peak.

target material	Scan type	C_e (counts)	C_m (counts)	C_m / C_e
Cd	Row	596	851	1.43 ± 0.42
Cd	Chip	38 134	51 817	1.36 ± 0.40
Cu	Row	15 361	11 164	0.73 ± 0.27
Cu	Chip	98 310	81 254	0.83 ± 0.31
Fe	Row	263	301	1.14 ± 0.24
Fe	Chip	16 811	19 378	1.15 ± 0.24
Mo	Row	181	383	2.11 ± 0.45
Mo	Chip	11 606	23 090	1.99 ± 0.41
Pb	Row	3170	3940	1.24 ± 0.47
Pb	Chip	202 893	248 895	1.23 ± 0.46
W	Row	3243	3978	1.23 ± 0.36
W	Chip	207 539	252 577	1.22 ± 0.35

measurements agree with expectations yielding a ratio compatible with unity. This agreement is far from trivial, recapitulating that DECAL and HEXITEC differ not only in pixel size and number, but are also based on different sensitive materials (Si and CdTe), whose thicknesses differ by a factor of 10 (25 µm and 250 µm) and make use of diverse readout frequencies (40 MHz and 1.591 kHz). On average 30% more counts are measured with DECAL than expected. One reason for that is a systematic undervaluation of C_H due to the charge sharing correction of the HEXITEC detector, that has only been taken into account statistically. The signals of neighboring pixels during one clock cycle are summed up and can thus account for charge sharing between pixels. However, neighboring pixels that coincidentally detect two different photons at the same time are summed up, too. This procedure leads to an underestimation of the counts C_H and thus of C_e. A non-energy dependent fraction of the measured excess can be explained that way. In a similar way it is possible, that charge sharing occurs between neighboring DECAL pixels, which has not been accounted for and can hence lead to an increase of measured counts. Also it is possible that traversing photons that are absorbed in the silicon bulk can still be detected which would speak for a depletion zone slightly larger than the epitaxial layer. It is especially noteworthy, that the row and chip scans with the same target material are all compatible with each other and deviate at most 12% as for the case of copper. This speaks for the correct functionality of masking pixels in the row scan. The noise peak broadening when unmasking the whole chip as described in section 4.5 does not effect the absolute number of counts for threshold voltages outside of the noise peak.

6. Conclusion and Outlook

The requirements of calorimeters at future colliders include high granularity, excellent energy resolution and radiation hardness at affordable costs. The development of silicon sensors provide a potential technology for a digital electromagnetic calorimeter (DECAL), that relies on counting shower particles rather than detecting their energy depositions. The high granular DECAL sensor is a Depleted Monolithic Active Pixel Sensor (DMAPS) prototype consisting of 64×64 pixels with 55 µm pitch and an epitaxial layer of 25 µm that is expected to be fully depleted when a low bias voltage is applied. Its pixel readout comprises a comparator that detects a hit when the shaper output falls below a globally set threshold voltage. Only this binary information is readout per 40 MHz clock cycle. The reconfigurable readout groups the pixel hits in either 64 strips, each of size 1×64 pixels, or in four pads of size 16×64 pixels. Strip mode offers a better spacial resolution but is more limited in the number of hits per strip than pad mode. The understanding of the sensor functionalities has been first investigated based on background measurements. Reproducible measurement parameters are selected:

- **Pixel tuning.** A tuning routine is developed that utilizes the six bit tuning DACs of each pixel to align the shaper outputs of all pixels. This is necessary because the threshold voltage can only be set globally. Within one row, the voltage range of shaper outputs is reduced by a factor of 15 after tuning. This allows the summation of noise counts within one row, leading to a much narrower standard deviation of 2.7 mV, compared to 12.8 mV before tuning.

- **Choice of currents within pixel electronics.** The current values of the shaper bias current, the preamplifier bias current and the feedback bias current have all been set to 100 µA. This setting was shown to favor large counts through optimized amplification and shaping behaviour.

- **Description of undesired voltage drift and its mitigation.** A voltage drift of the shaper output is observed for all pixels which ideally should be kept constant. The average drift value is measured to be 18.92 mV/ms, requiring a regular reset of the voltages. Such a reset is undertaken every 3100 clock cycles. The frequency of the clock is 40 MHz, which means that just before resetting, the shaper outputs have drifted by 0.73 mV on average. A dependence between drift and tuning DAC value has been found, but the exact cause of the drift still remains unexplained. This needs further investigation as the voltage drift should be eliminated in a new sensor design.

- **Measurement stability due to heat equilibrium.** After the start of sensor operation, the shaper output approaches an equilibrium while an increase in temperature is observed. A repetitive scan over the sensor lasting five minutes is sufficient to keep the voltage offset of the shaper output less than 0.5 mV away from their equilibrium value. Such an equalibrating scan is performed before every measurement taking.

- **Noise peak broadening.** It was found that the width of the noise peak per strip depends on the total number of unmasked strips. The standard deviation of a noise peak from a single unmasked strip doubles when comparing it in the environment of no to all other strips being unmasked. This is observed under high occupancy only, when most pixels detect a hit, because their digital readout components are all active. For a threshold voltage outside of the noise peak the pixels detect hits only when a traversing particle deposits a charge. The high granularity of the pixel sensor has the consequence that only a small fraction of pixels detect a particle hit simultaneously. This way the additional noise broadening does not emerge for signal measurements.

Based on the measurement parameters defined as above, the main goal of this thesis is discussed here. The DECAL sensor is characterized using incident photons in an energy range of 4-60 keV. Two energy calibration methods are developed. The first method parametrizes the DECAL threshold scans using error function fits. A signal height μ_{S} is obtained through these fits relative to the mean of the background noise peak. Relating this signal height to the characteristic fluorescence peak energy yields an energy calibration, compatible with a linear model. Its gradient m describes the signal height per unit energy as

$$m = 5.51 \pm 0.52\,\mathrm{mV/keV}. \tag{41}$$

A second calibration method builds upon a comparison measurement with the HEXITEC detector [40]. This detector is optimised for the X-ray detection in the energy range of 4-200 keV. Its energy spectra serve as the shape for the fit function to the DECAL energy spectra. A signal height per unit energy

$$a = 5.54 \pm 0.37\,\mathrm{mV/keV} \tag{42}$$

is obtained as the average over six independent results and is compatible with the result of the first calibration method. The agreement confirms the assumption of a linear dependence between signal height and photon energy up to 60 keV. The signal height can be expressed as the voltage obtained per produced electron-hole pair. The so-called conversion gain yields

$$\mathrm{c_g} = 19.95 \pm 1.32\,\mathrm{\mu V/e^-}, \tag{43}$$

and agrees with results already published in [29]. Additionally, the whole spectral data allows the estimation of the relative energy resolution as

$$\frac{\sigma_{\mathrm{E}}}{\mathrm{E}} = 12.2 \pm 3.5\%. \tag{44}$$

The resolution includes fluctuations in the electron-hole pair creation, in the charge collection and in the signal amplification and shaping.

Another important aspect of the sensor characterization is to investigate the absolute number of counts measured with the DECAL sensor. A comparison with the HEXITEC detector optimized for X-ray detection yields an agreement between DECAL counts and expectations. As a result, the photon absorption is considered to happen within the whole epitaxial layer, speaking for its full depletion. What is more, the independent measurements of single row and whole sensor scans are all compatible with each other. This substantiates the assumption that the DECAL pixels are considered independent when operated at threshold voltages outside of the noise peak regardless of other pixels being masked or unmasked. Altogether, the photon measurement with the DECAL sensor based on absorption in the energy range of 4-60 keV is understood. All pixels are tunable and sensitive with a count rate as expected for a fully depleted epitaxial layer.

In the future, further characterization of the DECAL sensor can be performed. The following measurements are proposed to improve the understanding of the DECAL sensor:

1. **Triggered strontium-90 scan.** A key characteristic of a detector in high energy physics is the sensitivity to a minimum ionizing particle (MIP). This can be best tested with an electron or proton test beam, as it offers good spacial alignment and monoenergetic particles at high fluence. Alternatively, a strontium-90 source can be used. A setup is proposed that triggers on the high energetic electrons from the strontium β-decay, that pass the sensor. Their energy deposition is expected to follow a Landau distribution. For a well functioning ECAL sensor, the most probable value of the distribution must be separated from the noise peak. The energy deposition of a MIP in the 25 µm thick silicon epitax is estimated through eq. (6) to be equivalent to the absorption of a 5.93 keV photon. The corresponding signal height is expected to be around 32.8 mV according to the energy calibration and should lie outside of the noise peak. This needs experimental verification.

2. **Source of voltage drift.** The shaper output of each pixel drifts with time. The search for the source of this voltage drift is still ongoing. Having found a dependence on the tuning DAC value, the tuning component of the readout needs to be investigated more thoroughly. A dependence between voltage drift and calibration DAC current is to be examined. Another good candidate for causing the drift is an unstable shaper bias current. The current was observed to shift the noise peak. Consequently, a drift of the current implies a drift of the shaper output.

3. **Improvement of time sensitivity.** As a mitigation of the described voltage drift, a pixel reset is performed frequently based on running a C++ script for measurement taking. A latency time between PC and FPGA board is detected that adds to the reset time in which the DECAL sensor is not sensitive. An improvement could be to implement the pixel reset on the FPGA board itself via a firmware update.

4. **Reduction of noise peak broadening.** Under high occupancy, the shaper outputs of all pixels fluctuate due to high digital activity in the readout. This environment only occurs for threshold voltages close to the noise peak. Nevertheless, a change in the readout circuit is sought to reduce the fluctuation. For a cleaner voltage input an additional capacitor per pixel readout could be beneficial to filter out the noise contribution from the voltage supply. As another alternative, the voltage supplies for the analog and digital front-end could be separated if the chip design allows.

5. **Charge sharing between neighboring pixels.** So far charge sharing between neighboring DECAL pixels is not taken into account. A statistical analysis will lead to an estimate of the frequency of which charge sharing happens. It would be interesting to conduct a correlation analysis of whether neighboring pixels detect photons with increased probability during the same clock cycle than further separated pixels. Additionally, the angle between particle source and sensor cross section can be varied to discriminate between charge sharing and a particle traversing multiple pixels.

6. **Source measurements in pad mode.** The digital summing logic of the pad mode has been verified as well as the behaviour under laser illumination [34]. However, all X-ray measurements so far have been performed in strip mode because it offers better spacial resolution. The firmware programmed to the FPGA board requires an update to handle the data structure corresponding to pad mode. While this is expected to function, it needs verification nevertheless by testing whether the absolute counts in strip and pad mode coincide.

The results from the tests proposed above may enter a new chip design. From this design it would be of high interest to build a multi-layered detector prototype. Such a prototype has the aim of reconstructing the third spacial dimension and detecting the formation of secondary particles. It is therefore necessary to simulate the setup with different absorber thicknesses and materials and compare with the measured counts. After testing with radioactive sources, the best way to characterize the detector prototype is a test beam that has sufficient energy to form electromagnetic showers. The reconstruction of initial particle energy can be compared to existing ECAL systems in terms of energy and spacial resolution. This offers insight into the experimental realization of a DECAL and its potential performance at high energy experiments.

A. DECAL threshold scans under X-ray fluorescence

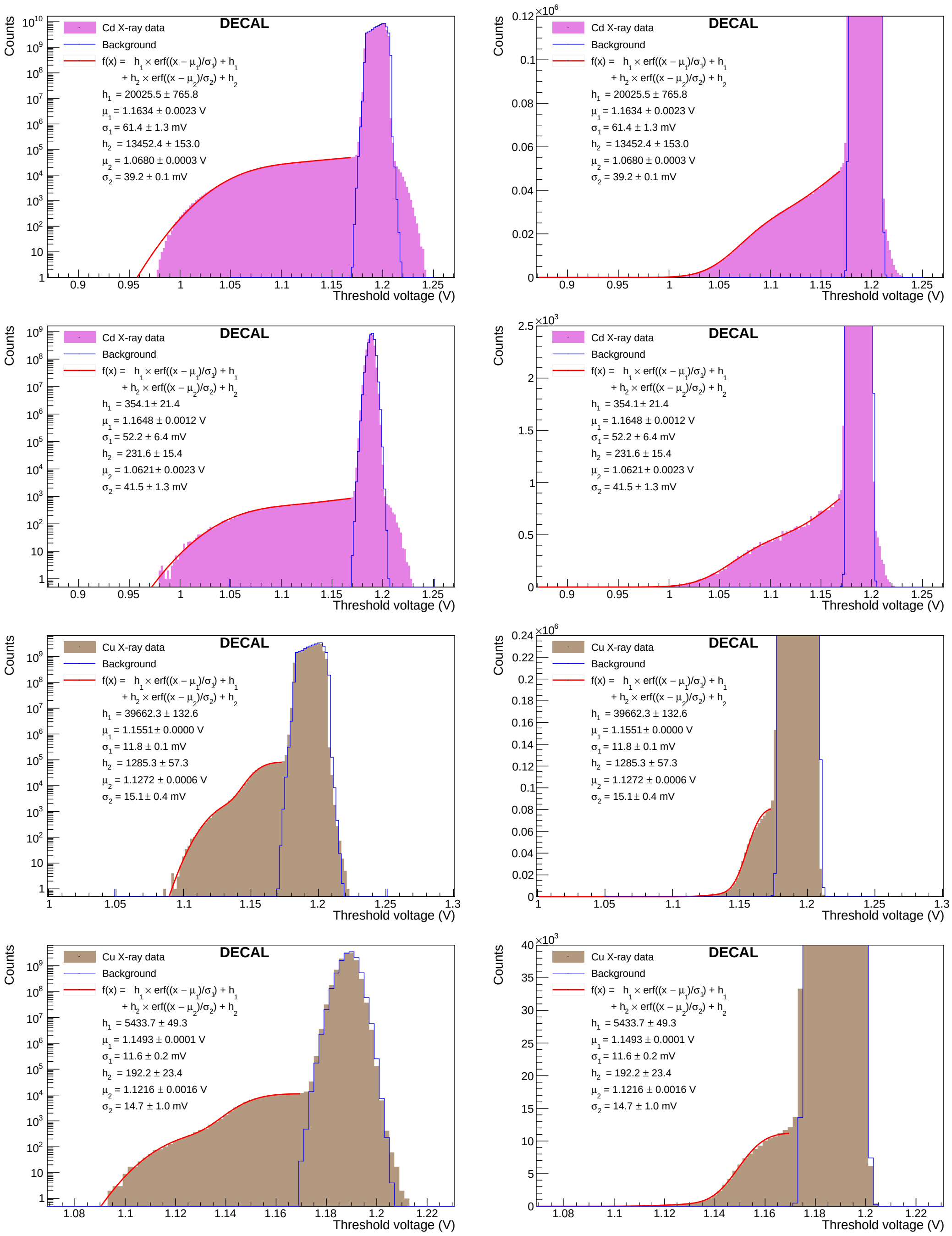

Figure 29: DECAL threshold scan under X-ray fluorescence of target materials Cd (**top four**) and Cu (**bottom** four). Left plots are the data on logarithmic y-axis and right plots on linear axis. First and third row show data of whole chip enabled and second and fourth the data of just row 32 enabled. The red lines are error function fits to the data.

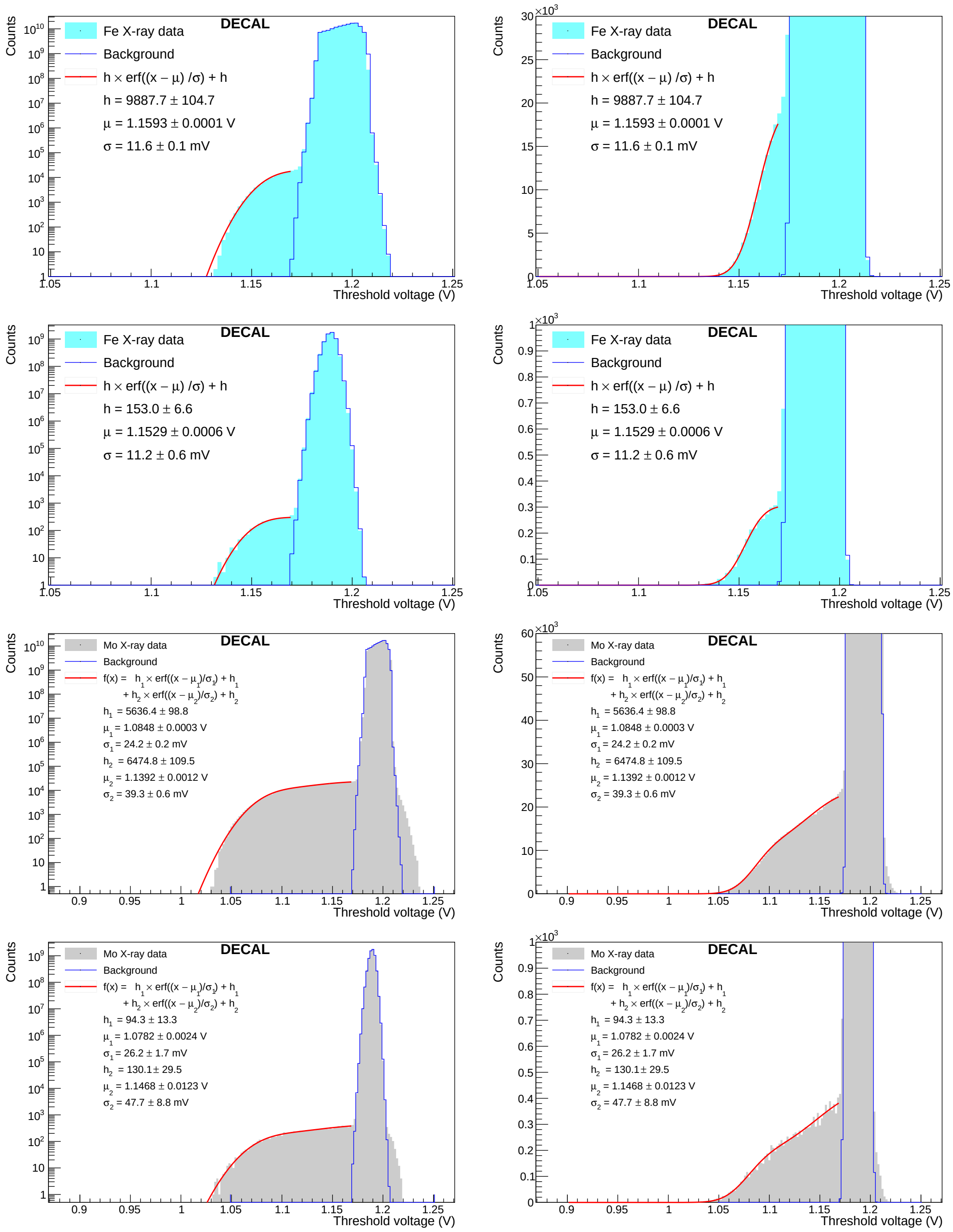

Figure 30: DECAL threshold scan under X-ray fluorescence of target materials Fe (**top four**) and Mo (**bottom four**). Left plots are the data on logarithmic y-axis and right plots on linear axis. First and third row show data of whole chip enabled and second and fourth the data of just row 32 enabled. The red lines are error function fits to the data.

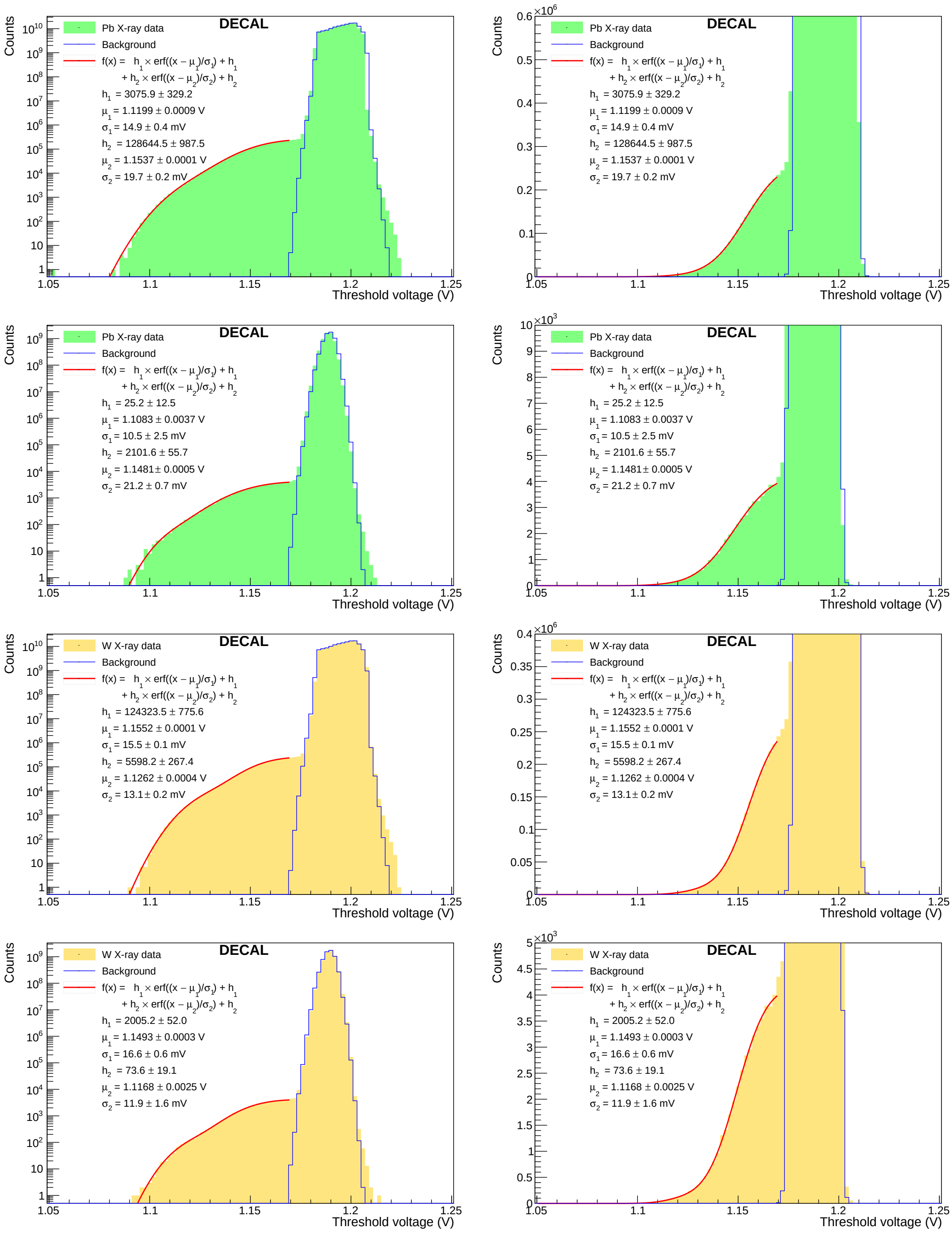

Figure 31: DECAL threshold scan under X-ray fluorescence of target materials Pb (**top four**) and W (**bottom four**). Left plots are the data on logarithmic y-axis and right plots on linear axis. First and third row show data of whole chip enabled and second and fourth the data of just row 32 enabled. The red lines are error function fits to the data.

Acronyms

ALICE A Large Ion Collider Experiment. 19

ATLAS A Toroidal LHC Apparatus. 18, 19

CMOS Complementary metal-oxide-semiconductor. 23

CMS Compact Muon Solenoid. 18–20

DAC Digital-to-analog converter. 29, 63

DECAL digital electomagnetic calorimeter. 9, 19, 66

DMAPS Depleted Monolithic Active Pixel Sensor. 9, 23

ECAL electromagnetic calorimeter. 9, 11, 17, 18, 65, 66

FPGA field-programmable gate array. 27, 28

HEXITEC High energy X-ray imaging technology. 46, 64, 65

HGCAL High-granularity calorimeter. 19

HL-LHC High Luminosity LHC. 18–20, 23

ITSDAQ ITk Strips Data Acquisition. 28

LHC Large Hadron Collider. 9

LVDS low-voltage differential signaling. 27, 28

MAPS Monolithic Active Pixel Sensor. 21, 23

MIP minimum ionizing particle. 11–13, 20, 46, 65

MPV most probable value. 46

RAL Rutherford Appleton Laboratory. 10, 41, 46, 47

SNR signal-to-noise ratio. 10, 23, 25

TCT Transient Current Technique. 25, 34

References

[1] R. Wigmans, Calorimetry: Energy Measurement in Particle Physics. Oxford University Press, 2017, ISBN: 9780198786351. DOI: 10.1093/oso/9780198786351.001.0001.

[2] P. Dauncey *et al.*, Performance of CMOS sensors for a digital electromagnetic calorimeter, *PoS (ICHEP 2010)*, vol. 502, 2010. DOI: 10.22323/1.120.0502.

[3] Particle Data Group, Review of particle physics, *Prog. Theor. Exp. Phys.*, 083C01, 2022. DOI: 10.1093/ptep/ptac097.

[4] C. Leroy and P.-G. Rancoita, Principles of radiation interaction in matter and detection, 4th edition. World Scientific, 2016, ISBN: 9789814603188.

[5] Y.-S. Tsai, Pair production and bremsstrahlung of charged leptons, *Rev. Mod. Phys.*, vol. 46, pp. 815–851, 1974. DOI: 10.1103/RevModPhys.46.815.

[6] M. Berger, J. Coursey, M. Zucker, *et al.*, Stopping-Power & Range Tables for Electrons, Protons, and Helium Ions, NIST Standard Reference Database Number 124. National Institute of Standards and Technology, Gaithersburg MD, 2017. DOI: 10.18434/T4NC7P.

[7] L. Rossi, P. Fischer, T. Rohe, *et al.*, Pixel Detectors, From Fundamentals to Applications. Springer-Verlag, 2006, ISBN: 3-540-28332-3. DOI: 10.1007/3-540-28333-1.

[8] M. Berger, XCOM: Photon cross section database, *National Institute of Standards and Technology, Gaithersburg, MD*, 1999. DOI: 10.18434/T48G6X.

[9] The ATLAS Collaboration, The ATLAS Experiment at the CERN Large Hadron Collider, *JINST*, vol. 3 (08), S08003, 2008. DOI: 10.1088/1748-0221/3/08/S08003.

[10] M. Aleksa, M. Diemoz, *et al.*, Discussion on the electromagnetic calorimeters of ATLAS and CMS, *Nucl. Instrum. Meth. A*, vol. 732, pp. 442–450, 2013. DOI: 10.1016/j.nima.2013.05.195.

[11] F. Cavallari, Performance of calorimeters at the LHC, *J. Phys.: Conf. Ser.*, vol. 293, 012001, 2011. DOI: 10.1088/1742-6596/293/1/012001.

[12] The CMS Collaboration, The CMS experiment at the CERN LHC, *JINST*, vol. 3, S08004, 2008. DOI: 10.1088/1748-0221/3/08/S08004.

[13] The CMS Collaboration, The CMS ECAL Phase-2 upgrade for high precision energy and timing measurements, *Nucl. Instrum. Meth. A*, vol. 958, 2020. DOI: 10.1016/j.nima.2019.04.113.

[14] The CMS Collaboration, Particle-flow reconstruction and global event description with the CMS detector, *JINST*, vol. 12 (10), P10003, 2017. DOI: 10.1088/1748-0221/12/10/P10003.

[15] The CMS Collaboration, The CMS high granularity calorimeter for the High Luminosity LHC, *Nucl. Instrum. Meth. A*, vol. 1041, 167312, 2022. DOI: 10.1016/j.nima.2022.167312.

[16] M. Šuljić, ALPIDE: the Monolithic Active Pixel Sensor for the ALICE ITS upgrade, *JINST*, vol. 11, C11025, 2016. DOI: 10.1088/1748-0221/11/11/C11025.

[17] A. de Haas, G. Nooren, T. Peitzmann, *et al.*, The FoCal prototype—an extremely fine-grained electromagnetic calorimeter using CMOS pixel sensors, *JINST*, vol. 13 (01), P01014, 2018. DOI: 10.1088/1748-0221/13/01/P01014.

[18] E. Rocco, Highly granular digital electromagnetic Calorimeter with MAPS, *Nucl. Part. Phys. Proc.*, vol. 273-275, pp. 1090–1095, 2016. DOI: 10.1016/j.nuclphysbps.2015.09.171.

[19] T. Peitzmann, J. Alme, R. Barthel, *et al.*, Results from the EPICAL-2 ultra-high granularity electromagnetic calorimeter prototype, *Nucl. Instrum. Meth. A*, 167539, 2022. DOI: 10.1016/j.nima.2022.167539.

[20] W. Snoeys, G. Aglieri Rinella, H. Hillemanns, *et al.*, A process modification for CMOS monolithic active pixel sensors for enhanced depletion, timing performance and radiation tolerance, *Nucl. Instrum. Meth. A*, vol. 871, pp. 90–96, 2017. DOI: 10.1016/j.nima.2017.07.046.

[21] H. Pernegger, Depleted CMOS sensors for HL-LHC, *PoS*, vol. VERTEX2018, p. 41, 2019. DOI: 10.22323/1.348.0041.

[22] R. Turchetta, Complementary metal-oxide-semiconductor (CMOS) sensors for high-performance scientific imaging, in *High Performance Silicon Imaging*, Woodhead Publishing, 2014, ISBN: 978-0-85709-598-5. DOI: 10.1533/9780857097521.2.281.

[23] C. J. Kenney, S. I. Parker, V. Z. Peterson, *et al.*, A prototype monolithic pixel detector, *Nucl. Instrum. Meth. A*, vol. 342 (1), pp. 59–77, 1994. DOI: 10.1016/0168-9002(94)91411-7.

[24] G. Claus, C. Colledani, W. Dulinski, *et al.*, Particle tracking using CMOS monolithic active pixel sensor, *Nucl. Instrum. Meth. A*, vol. 465, pp. 120–124, 2001, SPD2000. DOI: 10.1016/S0168-9002(01)00368-0.

[25] I. Perić, A novel monolithic pixelated particle detector implemented in high-voltage CMOS technology, *Nucl. Instrum. Meth. A*, vol. 582 (3), pp. 876–885, 2007, VERTEX 2006. DOI: 10.1016/j.nima.2007.07.115.

[26] M. Munker, M. Benoit, D. Dannheim, *et al.*, Simulations of CMOS pixel sensors with a small collection electrode, improved for a faster charge collection and increased radiation tolerance, *JINST*, vol. 14, C05013, 2019. DOI: 10.1088/1748-0221/14/05/c05013.

[27] B. Hiti, L. Simon Argemi, I. Asensi Tortajada, *et al.*, Development of the monolithic MALTA CMOS sensor for the ATLAS ITk outer pixel layer, in *TWEPP2018*, vol. 343, 2019. DOI: 10.22323/1.343.0155.

[28] The ALICE Collaboration, ALPIDE, the Monolithic Active Pixel Sensor for the ALICE ITS upgrade, *Nucl. Instrum. Meth. A*, vol. 824, pp. 434–438, 2016. DOI: 10.1016/j.nima.2015.09.057.

[29] P. Allport, S. Benhammadi, R. Bosley, *et al.*, DECAL: A Reconfigurable Monolithic Active Pixel Sensor for Tracking and Calorimetry in a 180 nm Image Sensor Process, *Sensors*, vol. 22 (18), 2022. DOI: 10.3390/s22186848.

[30] G. Lutz *et al.*, Semiconductor radiation detectors. Springer, 2007, ISBN: 978-3-540-71678-5.

[31] S. Sze, Semiconductor devices: Physics and technology. John wiley & sons, 2008, ISBN: 978-0-470-53794-7.

[32] H. Spieler, Front-End Electronics and Signal Processing, in *AIP Conference Proceedings*, American Institute of Physics, vol. 674, 2003, pp. 76–100. DOI: 10.1063/1.1604074.

[33] F. Krummenacher, Pixel detectors with local intelligence: An IC designer point of view, *Nucl. Instrum. Meth. A*, vol. 305 (3), pp. 527–532, 1991. DOI: 10.1016/0168-9002(91)90152-G.

[34] P. Allport, R. Bosley, J. Dopke, *et al.*, First tests of a reconfigurable depleted maps sensor for digital electromagnetic calorimetry, *Nucl. Instrum. Meth. A*, vol. 958, 162654, 2020. DOI: 10.1016/j.nima.2019.162654.

[35] S. Benhammadi, J. Dopke, N. Guerrini, *et al.*, DECAL: A Reconfigurable Monolithic Active Pixel Sensor for use in Calorimetry and Tracking, in *TWEPP*, 2019. DOI: 10.22323/1.370.0040.

[36] The ATLAS Collaboration, “Technical Design Report for the ATLAS Inner Tracker Strip Detector,” CERN, Geneva, Tech. Rep., 2017. DOI: 10.3204/PUBDB-2017-09975.

[37] I. Kopsalis, P. Allport, S. Benhammadi, *et al.*, Evaluation of the DECAL Fully Depleted monolithic sensor for outer tracking and digital calorimetry, *Nucl. Instrum. Meth. A*, vol. 1038, 2022. DOI: 10.1016/j.nima.2022.166955.

[38] M.-M. Bé, V. Chisté, C. Dulieu, *et al.*, Table of Radionuclides Volume 2, 2004.

[39] A. Chetham-Strode and E. M. Kinderman, The Half-Life of Yttrium-90, *Phys. Rev.*, vol. 93, pp. 1029–1029, 5 1954. DOI: 10.1103/PhysRev.93.1029.

[40] Quantum detectors Ltd, RAL, Harwell, UK, High energy X-ray imaging technology detector, https://quantumdetectors.com/products/hexitec/, Accessed: 2022-11-18.

[41] A. Thompson, D. Attwood, E. Gullikson, *et al.*, X-ray data booklet, *Berkeley, CA*, 2009, https://xdb.lbl.gov/xdb-new.pdf, Accessed: 2022-11-18.

Acknowledgements

Ich möchte mich bei Cigdem Issever und Klaus Mönig für die Betreuung der Arbeit bedanken. Die regelmäßigen Treffen mit Cigdem Issever, Marie Sturm, Hannsjörg Weber und Steven Worm haben stets zu fruchtbaren Diskussionen geführt und Freude sowie Motivation gestiftet. Insbesondere danke ich Hannsjörg für den engen Austausch über die physikalischen Fragestellungen dieser Arbeit und die Freude am Experimentieren. Das vertrauensvolle Arbeitsverhältnis habe ich genauso wie die lehrreichen Anmerkungen zu Analysen, Präsentationen und zur Korrektur dieser Arbeit sehr wertgeschätzt.

Beim Aufbau des Labors war Olf Epler grundlegend. Von Kabeln bis Computern hat er uns versorgt. Yulia Jagodzinski hat nicht nur Klarheit in zahlreiche meiner Fragen gebracht sondern auch den Zusammenhalt während der Pandemie innerhalb der Forschungsgruppe gestärkt. Sommer- und Weihnachtsfeste haben besonders viel Spaß bereitet.

Ich danke Ingo Bloch für die Gewährleistung des Strahlenschutzes beim Hantieren mit der Americium-Quelle am DESY Zeuthen. Also thanks to Vlad for making space in his lab area.

Zu Beginn der Masterarbeit hat Jens Dopke mit viel Geduld die ersten Messversuche begleitet und stand auch danach noch mit klarem Feedback und Ideen zur Stelle. I enjoyed the meetings with the whole DECAL collaboration and appreciated the interest and feedback. Iain Sedgwick gave lots of crucial feedback regarding the sensor design, that I found extremely helpful.

A highlight was the trip to Oxford and RAL for which I'm very grateful. Thanks are due to Ioannis Kopsalis for the daily guidance and building the bridge to the local scientists. We thank Sion Richards and Matt Wilson for granting access and providing support to the X-ray tube facilities and to the HEXITEC detector of the Technology Department at STFC-RAL. Again thanks to Jens for welcoming us with lasagne and drinks, when distraction from the lab work was needed.

Also, I would like to thank Heiko Lacker for introducing me to experimental particle physics in his lectures and gathering kind people at the institute. Thanks Alessia, Andrew, Anupama, Doramas and Jakob for many refreshing breaks and activities.

Selbständigkeitserklärung

Ich erkläre hiermit, dass ich die vorliegende Arbeit selbständig verfasst und noch nicht für andere Prüfungen eingereicht habe. Sämtliche Quellen einschließlich Internetquellen, die unverändert oder abgewandelt wiedergegeben werden, insbesondere Quellen für Texte, Grafiken, Tabellen und Bilder, sind als solche kenntlich gemacht. Mir ist bekannt, dass bei Verstößen gegen diese Grundsätze ein Verfahren wegen Täuschungsversuchs bzw. Täuschung eingeleitet wird.

Berlin, den 21. November 2022 ....